

AD-A040 666

PENNSYLVANIA STATE UNIV UNIVERSITY PARK APPLIED RESE--ETC F/G 20/12
DOPPLER-SHIFTED ACOUSTIC CYCLOTRON RESONANCE IN INDIUM.(U)

MAR 73 S C HAYDEN

N00017-70-C-1407

UNCLASSIFIED

TN-73-35

NL

4 OF 24
AD
A040666



ADA 040666

(2) B.S.

(6)

DOPPLER-SHIFTED ACOUSTIC CYCLOTRON RESONANCE IN INDIUM.

(10)

Stephen C. Hayden

(11) 5 May 73

(9)

Doctoral thesis,

(12) 88p.

(14)

Technical Memorandum

File No. TM-73-35

March 5, 1973

Contract No. N00017-70-C-1407

(15)

Copy No. 5

DDC
RECEIVED
JUN 17 1977
C

The Pennsylvania State University
Institute for Science and Engineering
APPLIED RESEARCH LABORATORY
University Park, Pennsylvania

APPROVED FOR PUBLIC RELEASE
DISTRIBUTION UNLIMITED

NAVY DEPARTMENT

NAVAL ORDNANCE SYSTEMS COMMAND

AD No. 1
UDC FILE COPY

1473
391 007

1B

ABSTRACT

The Fermi surface of indium was investigated using the Doppler-shifted acoustic cyclotron resonance method. The measurements are sensitive to small changes in the shape of the Fermi surface and, hence, are a good measure of the deviations of the Fermi surface from the free-electron model.

The attenuation of short pulses of longitudinal sound, with a frequency between 100 MHz and 300 MHz, in single crystal indium was measured in the presence of a varying magnetic field. Values of the magnetic field at which peaks in the acoustic absorption were observed are related to the rate of change of the area of the cross section of the Fermi surface normal to the magnetic field with respect to the component of the electron wave-vector parallel to the magnetic field.

The shape of the Fermi surface of indium in the third Brillouin zone is in question. Most investigators have not observed the α -arms of the Fermi surface in the third zone predicted by the free-electron model. As a consequence, the existence of the α -arms has been considered doubtful. However, the observations of this investigation can be interpreted consistently only if the α -arms are assumed to exist.

A limited investigation was made of the dependence of the heights of the absorption resonance peaks on temperature, magnetic field and sonic wave number. The results of these measurements await the development of a general theory of Doppler-shifted acoustic cyclotron resonance for comparison with theoretical predictions.

Unclassified

Security Classification

DOCUMENT CONTROL DATA - R & D

(Security classification of title, body of abstract and indexing annotation must be entered when the overall report is classified)

1. ORIGINATING ACTIVITY (Corporate author) Applied Research Laboratory University Park, Pennsylvania		2a. REPORT SECURITY CLASSIFICATION Unclassified	
3. REPORT TITLE Doppler-Shifted Acoustic Cyclotron Resonance in Indium		2b. GROUP	
4. DESCRIPTIVE NOTES (Type of report and inclusive dates) Ph.D. Thesis, Physics, June 1973			
5. AUTHOR(S) (First name, middle initial, last name) Stephen C. Hayden			
6. REPORT DATE March 5, 1973		7a. TOTAL NO. OF PAGES 85	7b. NO. OF REFS 25
8a. CONTRACT OR GRANT NO. N00017-70-C-1407		9a. ORIGINATOR'S REPORT NUMBER(S) TM 73-35	
b. PROJECT NO.		9b. OTHER REPORT NO(S) (Any other numbers that may be assigned this report)	
c.			
d.			
10. DISTRIBUTION STATEMENT Approved for public release. Distribution unlimited. Per NAVORD - April 3, 1973			
11. SUPPLEMENTARY NOTES		12. SPONSORING MILITARY ACTIVITY Naval Ordnance Systems Command Department of the Navy	
13. ABSTRACT The Fermi surface of indium was investigated using the Doppler-shifted acoustic cyclotron resonance method. The measurements are sensitive to small changes in the shape of the Fermi surface and, hence, are a good measure of the deviations of the Fermi surface from the free-electron model. The attenuation of short pulses of longitudinal sound, with a frequency between 100 MHz and 300 MHz, in single crystal indium was measured in the presence of a varying magnetic field. Values of the magnetic field at which peaks in the acoustic absorption were observed are related to the rate of change of the area of the cross section of the Fermi surface normal to the magnetic field with respect to the component of the electron wave-vector parallel to the magnetic field. The shape of the Fermi surface of indium in the third Brillouin zone is in question. Most investigators have not observed the α -arms of the Fermi surface in the third zone predicted by the free-electron model. As a consequence, the existence of the α -arms has been considered doubtful. However, the observations of this investigation can be interpreted consistently only if the α -arms are assumed to exist. A limited investigation was made of the dependence of the heights of the absorption resonance peaks on temperature, magnetic field and sonic wave number. The results of these measurements await the development of a general theory of Doppler-shifted acoustic cyclotron resonance for comparison with theoretical predictions.			

DD FORM 1 NOV 65 1473

(PAGE 1)

PLATE NO. 21856

Unclassified

Security Classification

8/N 0102-014-6600

Unclassified

Security Classification

14. KEY WORDS	LINK A		LINK B		LINK C	
	ROLE	WT	ROLE	WT	ROLE	WT
ACOUSTIC CYCLOTRON	8					
ATTENUATION	8					
BRILLOUIN ZONE	8					
DOPPLER	8					
FERMI SURFACE	8					
INDIUM	8					
MAGNETIC FIELD	8					
RESONANCE	8					

DISTRIBUTION

Commander (ORD 632)
Naval Ordnance Systems Command
Department of the Navy
Washington, D. C. 20360

Copies 1 and 2

Commander (ORD 34B)
Naval Ordnance Systems Command
Department of the Navy
Washington, D. C. 20360

Copies 3 and 4

Defense Documentation Center
5010 Duke Street
Cameron Station
Alexandria, Virginia 22314

Copies 5 through 16

Via: Commander (ORD 632)
Naval Ordnance Systems Command
Department of the Navy
Washington, D. C. 20360

ACKNOWLEDGMENTS

The author thanks Professor F. G. Brickwedde for suggesting this investigation and for his interest, assistance and encouragement during its course.

The author wishes to express his gratitude to Dr. Robert W. Reed, Assistant Professor of Physics, for his interest in this investigation and his generous assistance in the construction and operation of the experimental apparatus.

Assistance from Dr. George D. Whitfield, Associate Professor of Physics, with understanding the theory is acknowledged.

Permission to use the spark cutting machine for forming the specimens essential to this research was kindly granted by Professor Gerd Rosenblatt, Department of Chemistry, and was greatly appreciated.

The author is indebted to Mr. Edward F. Vozenilak for performing the resistance-ratio measurements on the specimens and for his generous assistance in the recording of the data.

Grants of graduate assistantships to the author during this investigation by the Applied Research Laboratory and The Pennsylvania State University were appreciated.

This investigation was supported by the Applied Research Laboratory of The Pennsylvania State University under contract with the Naval Ordnance Systems Command.

A	ACCESSION	FILE
	NO.	DATE
	CLASSIFIED	BY
	JUSTIFICATION	DATE
BY	DISTRIBUTION / AVAILABILITY CODES	
NO.	AVAIL. CODE / SPECIAL	

TABLE OF CONTENTS

	Page
ACKNOWLEDGMENTS	ii
LIST OF TABLES	iv
LIST OF FIGURES	v
TABLE OF SYMBOLS	vii
I. INTRODUCTION	1
II. THEORY	3
III. EXPERIMENTAL APPARATUS AND TECHNIQUES	17
Method Employed for Measuring Ultrasonic Attenuation in the Presence of a Magnetic Field	17
Apparatus for Measuring Doppler-Shifted Acoustic Cyclotron Resonance	18
Specimen Preparation	29
Specimen Bonding	32
IV. MODEL OF INDIUM FERMI SURFACE	33
V. EXPERIMENTAL RESULTS	43
The Data	43
Analysis of the Data	45
Comparison of the Results with Models of the Fermi Surface of Indium	50
Dependence of the DSACR Attenuation on Temperature, Magnetic Field and Sonic Frequency	59
VI. SUMMARY, CONCLUSIONS AND SUGGESTIONS FOR FUTURE WORK . .	67
Suggestions for Future Work	68
APPENDIX A	
Properties of Indium	70
APPENDIX B	
Fast Fourier Transform	72
FOOTNOTES	75
BIBLIOGRAPHY	77

LIST OF TABLES

Table	Page
I. Experimental values of R_{\max} along axes of crystal symmetry	49
II. Information pertinent to the investigation of the dependence of Δ/Δ_0 on temperature and magnetic field	65

LIST OF FIGURES

Figure	Page
1. Electron orbits on the Fermi surface in planes normal to k_z for $k_z = \text{constant}$ and $(k_z + \delta k_z) = \text{constant}$	7
2. A plot of R vs k_z for a hypothetical Fermi surface . . .	12
3. A plot of the sonic attenuation, α , vs. $1/H$ showing the behavior expected from the theory	16
4. Multi-ramp sweep unit used to provide the ramp to the magnet power supply	20
a. Digital counter with latched output	20
b. Programmable integrator	21
5. Block diagram of the electronic part of the apparatus used to measure the ultrasonic attenuation	23
a. Acoustic signal section	23
b. Automatic gain control section	24
c. Timing section	25
d. Recording section	26
6. High-speed sample and hold circuit with variable gate and delayed trigger	28
7. The first Brillouin zone of indium	34
8. The free-electron model of the Fermi surface of indium .	35
9. R_{max} on the second-zone hole surface of indium calculated using the OSA model	37
10. Calculated values of R_{max} using the free-electron model in the third zone	41
11. A plot of echo-height vs. magnet current from the X-Y recorder	44
12. A Calcomp plot used in the determination of periodicity in $1/H$	47
13. Values of R_{max} , calculated from the experimental data, plotted against θ , the angle between \vec{q} and \vec{H}	48

LIST OF FIGURES (cont.)

Figure	Page
14. Projections of the free-electron third-zone Fermi surface on crystal planes	53
a. (010) plane	53
b. (001) plane	54
c. (110) plane	55
15. Normalized height of the absorption peak, Δ/Δ_0 , vs. temperature	60
16. The normalized height of the absorption peaks, Δ/Δ_0 , on a logarithmic scale vs. the order number, n , of the peaks	61
17. The normalized height of the absorption peaks, Δ/Δ_0 , vs. sonic wave number, q	62

TABLE OF SYMBOLS

A	cross-sectional area of the Fermi surface
c	speed of light
e	electronic charge
ϵ	energy
ϵ_F	Fermi energy
ϵ_λ	Landau energy
f	sonic frequency
\hbar	Planck's constant divided by 2π
\vec{H}	magnetic field intensity
\vec{k}	electron wave vector
ℓ	electron mean-free-path
λ	Landau level quantum number
m_{ij}^*	(i,j) component of the effective mass tensor
m_c	cyclotron mass
n	order number of resonance peaks
ω	sonic angular frequency
ω_c	cyclotron angular frequency
ω_{eff}	effective sonic angular frequency
\vec{q}	sonic wave vector
R	$\frac{1}{2\pi} \left \frac{\partial A(k_z)}{\partial k_z} \right $
T	temperature
v_F	Fermi velocity
v_s	ultrasonic wave velocity

CHAPTER I

INTRODUCTION

Investigations of the Fermi surface of metals have become an active area of research over the past several years. These studies are important since most of the electronic properties of a metal are related to the topology of the Fermi surface. A reason for this is that the conduction electrons that participate in electronic processes, in general, reside on or near the Fermi surface. The crystalline anisotropy in the electronic properties of metals is related to the anisotropy of the Fermi surface and the electron effective masses and velocities are directly related to the topology of the Fermi surface.

The Fermi surface is used in the explanation of several experimentally observed effects such as the de Haas-van Alphen oscillations in the magnetic susceptibility, the Sondheimer oscillations in the magnetoresistance, and various types of magnetoacoustic effects. Conversely, these effects can be used as effective tools in gauging the Fermi surface. For example, the de Haas-van Alphen effect and magnetoacoustic quantum oscillation measurements yield areas of extremal cross section of the Fermi surface and the low field magnetoacoustic effect yields extremal radii.

Another type of magnetoacoustic measurement, called Doppler-shifted acoustic cyclotron resonance (DSACR), can be used to measure the extremal values of the derivative of the cross-sectional area of the Fermi surface with respect to the component of the electron wave-vector in the direction of \vec{H} . This method provides additional

information about the topology of the Fermi surface which, in general, is more sensitive to small changes than that provided by other methods. DSACR measurements complement other types of measurement of the Fermi surface.

It is the purpose of this thesis to use DSACR to explore the Fermi surface of indium. A limited investigation of the effect of some experimental parameters on the acoustic absorption peaks due to DSACR is also done.

Indium was chosen for this investigation for two reasons. Indium is available in pure, single-crystal form and there has been a lack of agreement between various sets of reported data and several explanations offered for the marked deviations from the free-electron predictions. It is hoped that the additional measurements reported in the thesis will contribute to a resolution of these differences.

CHAPTER II

THEORY

A theory of Doppler-shifted acoustic cyclotron resonances has been given by several authors.¹⁻⁴ The theory is not reproduced here. Instead, the resonance condition is derived in terms of the free-electron model and a physical picture of DSACR is presented. The resonance condition derived here is the same as that of the detailed theory.

Consider the motion of a free electron in the presence of a magnetic field along the z-direction. The Schrödinger equation is

$$\frac{1}{2m^*} \left(\frac{\hbar \vec{\nabla}}{i} - \frac{e}{c} \vec{A} \right)^2 \psi(x, y, z) = \epsilon_\lambda \psi(x, y, z) \quad (1)$$

where e is the electronic charge, m^* is the effective mass of the electron which is, in general, a tensor

$$\frac{1}{m_{i,j}^*} = \frac{1}{\hbar^2} \frac{\partial^2 \epsilon(\vec{k})}{\partial k_i \partial k_j} \quad (2)$$

and \vec{A} is the vector potential, $(0, Hx, 0)$. The Schrödinger equation can be solved easily yielding an electron motion in the x-y plane with quantized energy levels, called Landau levels, given by

$$\epsilon_\lambda(k_z) = (\lambda + 1/2) \hbar \omega_c + \frac{\hbar^2 k_z^2}{2m^*} \quad (3)$$

where $\lambda = 0, 1, 2, \dots$.

The first term on the right side of Equation (3) is the cyclotron energy, where

$$\omega_c = \frac{eH}{m_c c} \quad (4)$$

is the cyclotron angular frequency. For a spherical Fermi surface, the cyclotron mass, $m_c = m^*$. However, for a general Fermi surface, m^* is not constant around the cyclotron orbit and m_c is defined by Equation (4).

Consider the case where an electron in the presence of a magnetic field changes Landau levels; i.e., λ in Equation (3) changes upon the absorption of a phonon with a wave vector \vec{q} . The conservation of energy and linear momentum in the direction of the magnetic field is expressed by

$$(\lambda_i + 1/2)\hbar\omega_c + \frac{\hbar^2 k_z^2}{2m^*} + \hbar\omega = (\lambda_f + 1/2)\hbar\omega_c + \frac{\hbar^2}{2m^*} (k_z + q_z)^2, \quad (5)$$

where ω is the phonon angular frequency and q_z the component of \vec{q} in the z-direction. Equation (5) is reducible to

$$n\omega_c + \omega = \frac{\hbar}{2m^*} q_z^2 + \frac{\hbar}{m^*} k_z q_z, \quad (6)$$

where $n = \lambda_f - \lambda_i$. For the highest sonic frequency used (300 MHz), $q = \omega/v_s = 3.27 \times 10^3 \text{ cm}^{-1}$. The radius of the free-electron sphere in reciprocal space, k_F , is $\sim 10^8 \text{ cm}^{-1}$. Therefore, for values of k_z such that $k_F \geq k_z \gg q_z$, the term in q_z^2 on the right hand side of Equation (6) may be neglected compared to the term in $k_z q_z$. Then, using the relation $v_z = \frac{\hbar}{m^*} k_z$, we find

$$n\omega_c + \omega = v_z q_z. \quad (7)$$

If the angle between \vec{H} and \vec{q} is θ , then $q_z = q \cos \theta$ so that

$$n\omega_c = v_z q \cos \theta - \omega = \omega \left(\frac{v_z}{v_s} \cos \theta - 1 \right), \quad (8)$$

where v_s is the sonic velocity appropriate to the direction of \vec{q} .

Introducing ω_{eff} :

$$\omega_{\text{eff}} = \omega \left(\frac{v_z}{v_s} \cos \theta - 1 \right), \quad (9)$$

the condition of absorption is

$$\omega_{\text{eff}} = n\omega_c \quad (10)$$

which is of the form for normal cyclotron resonance. Note that ω_{eff} is the Doppler-shifted sonic frequency seen in a reference frame moving with a speed v_z parallel to \vec{H} ; thus the name Doppler-shifted acoustic cyclotron resonance. Substituting $\omega_c = eH/m_c$ in Equation (10) and noting that $v_z \approx 10^8 \text{ cm/sec}$ while $v_s \approx 10^5 \text{ cm/sec}$ so that $\frac{v_z}{v_s} \cos \theta \gg 1$ if θ does not approach $\pi/2$, the resonance condition is closely approximated by

$$\frac{1}{H} = n \frac{ev_s}{c(m_c \bar{v}_z) \omega \cos \theta}. \quad (11)$$

Here, v_z has been replaced by \bar{v}_z , the average value of v_z around the cyclotron orbit, since, in general, v_z is not constant around the orbit.

The resonance condition is related to the topology of the Fermi surface through the product $m_c \bar{v}_z$. Consider the intersections of

planes normal to \vec{H} at k_z and at $(k_z + \delta k_z)$ with a general Fermi surface as shown in Figure 1. Both intersections correspond to electron orbits on the Fermi surface in reciprocal space with the Fermi energy, ϵ_F .

The point P on the orbit in the k_z equals a constant plane is translated to the point P' on the orbit in the $(k_z + \delta k_z)$ equals a constant plane by $\delta \vec{k}$. $\delta \vec{k}$ can be described by components $\delta \vec{k}_n$ normal to the orbit in \vec{k} -space, $\delta \vec{k}_t$ tangential to the orbit and $\delta \vec{k}_z$ in the \hat{k}_z -direction as shown in Figure 1. Since the energy corresponding to both orbits is the same, the change in energy, $\delta \epsilon = 0$. Then noting that $(\partial \epsilon / \partial k_z) = \hbar v_z$ and $v_t = 0$, since the electron velocity is normal to the orbits in reciprocal space, we can write

$$\delta \epsilon = \left(\frac{\partial \epsilon}{\partial k_t} \right) \delta k_t + \left(\frac{\partial \epsilon}{\partial k_n} \right) \delta k_n + \left(\frac{\partial \epsilon}{\partial k_z} \right) \delta k_z = 0 \quad (12)$$

or

$$\hbar v_n \delta k_n + \hbar v_z \delta k_z = 0 \quad (13)$$

Using the Lorentz Force equation,

$$\hbar \frac{d\vec{k}_\perp}{dt} = \left(\frac{e}{c} \right) \vec{v} \times \vec{H} \quad (14)$$

where $\vec{H} = (0, 0, H)$ and k_\perp is the component of \vec{k} perpendicular to \vec{H} , to eliminate v_n in Equation (13), we find

$$\frac{\hbar^2 c}{eH} \dot{k}_\perp \delta k_n + \hbar v_z \delta k_z = 0 \quad (15)$$

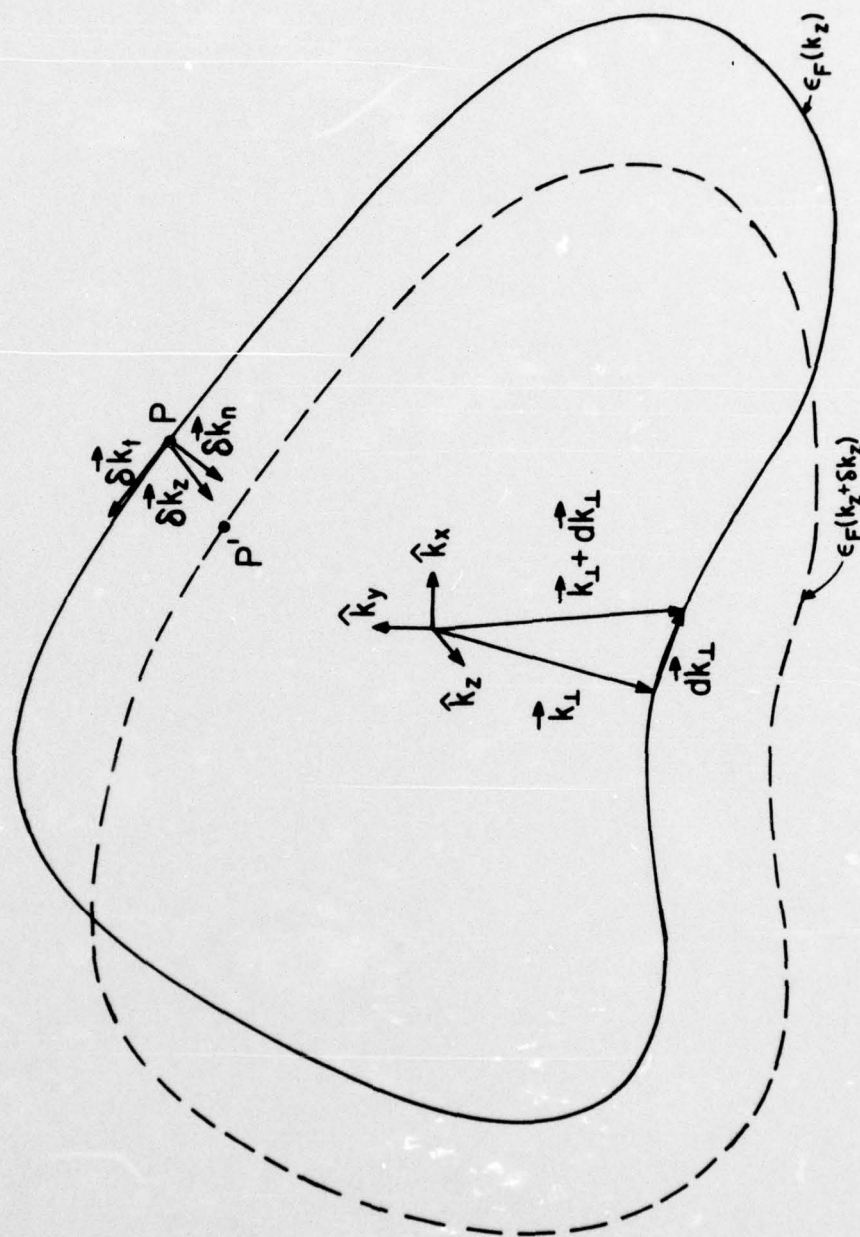


Figure 1. Electron orbits on the Fermi surface in planes normal to k_z for $k_z = \text{constant}$ and $(k_z + \delta k_z) = \text{constant}$.

Now take a time integral around the orbit:

$$\hbar \delta d_z \oint v_z dt + \frac{\hbar^2 c}{eH} \oint \delta k_n \dot{k}_1 dt = 0 \quad (16)$$

and note that

$$\oint v_z dt = \frac{2\pi}{\omega_c} \bar{v}_z \quad (17)$$

and

$$\omega_c = \frac{eH}{m_c} \quad (18)$$

In Figure 1 it can be seen that \vec{dk}_1 is in the \hat{k}_t -direction so that

$$\delta A = \oint_C \delta k_n dk_t = \oint \delta k_n \dot{k}_1 dt \quad (19)$$

where δA is the difference in the area enclosed by the orbits in the planes perpendicular to \vec{H} through k_z and $k_z + \delta k_z$. Substituting Equations (17), (18) and (19) into Equation (16) one has

$$2\pi m_c \bar{v}_z = \hbar \left| \frac{\partial A(k_z)}{\partial k_z} \right| \quad (20)$$

or

$$m_c \bar{v}_z = \hbar R \quad (21)$$

where

$$R \equiv \frac{1}{2\pi} \left| \frac{\partial A(k_z)}{\partial k_z} \right| \quad (22)$$

Substituting into Equation (11) we finally arrive at the desired resonance condition

$$\frac{1}{H} = n \frac{ev_s}{\hbar c \omega R \cos \theta} \quad (23)$$

The changing of Landau levels by an electron may be viewed as resulting from a perturbation by the sonic wave. The interaction arises from the induced electric field associated with the sonic wave and the deformation of the Fermi surface resulting from the compression and rarefaction of the ion cores. The perturbing potential, $U(\vec{r}, t)$, seen by the moving electrons may be written

$$U(\vec{r}, t) = u(\vec{r}) e^{-i\omega_{\text{eff}} t}, \quad (24)$$

where ω_{eff} is the effective angular frequency defined by Equation (9). Then, using first-order time-dependent perturbation theory, the probability that an electron in state $|\vec{k}\rangle$ at time = 0 will be in state $|\vec{k}'\rangle$ at time t is⁵

$$|a_{\vec{k}}^{\vec{k}', \vec{k}}(t)|^2 = \frac{4|u_{\vec{k}', \vec{k}}^{\vec{k}}|^2}{\hbar^2 (\omega_{\vec{k}', \vec{k}}^{\vec{k}} - \omega_{\text{eff}})^2} \sin^2 \left(\frac{(\omega_{\vec{k}', \vec{k}}^{\vec{k}} - \omega_{\text{eff}})}{2} t \right), \quad (25)$$

where $u_{\vec{k}', \vec{k}}^{\vec{k}}$ is the matrix element $\langle \vec{k}' | u(\vec{r}) | \vec{k} \rangle$ and $\hbar \omega_{\vec{k}', \vec{k}}^{\vec{k}}$ is the energy difference in the Landau levels of states $|\vec{k}'\rangle$ and $|\vec{k}\rangle$. $|a_{\vec{k}}^{\vec{k}', \vec{k}}(t)|^2$ is sharply peaked when $\omega_{\text{eff}} = \omega_{\vec{k}', \vec{k}}^{\vec{k}}$ which corresponds to the absorption condition expressed in Equation (9). The transition probability per unit time when $\omega_{\text{eff}} = \omega_{\vec{k}', \vec{k}}^{\vec{k}}$ is

$$\frac{2\pi}{\hbar} |\mathbf{u}_{\mathbf{k},\mathbf{k}'}|^2 N(\epsilon) , \quad (26)$$

where $N(\epsilon)$ is the energy density of states at \mathbf{k}' .

Consider first the interaction due to the induced oscillating electric field. For longitudinal sound with \vec{q} in the z-direction, the force on the electron due to the induced field is also in the z-direction. The energy of an electron in a magnetic field $\vec{H} = H\hat{z}$ on the Fermi surface is

$$\epsilon_F = \epsilon_\lambda + \epsilon_z , \quad (27)$$

where

$$\epsilon_\lambda = (\lambda + 1/2)\hbar\omega_c \text{ and } \epsilon_z = \frac{\hbar^2 k_z^2}{2m^*} . \quad (28)$$

If the frequency of the induced force as seen by an electron moving on a cyclotron orbit matches the variational frequency of v_z of the electron around the cyclotron orbit, which is ω_c , or $s\omega_c$ for an orbit of s -fold symmetry, the cyclotron motion of the electron is in phase with the oscillating perturbing potential arising from the sonic wave. This perturbation causes electrons to change their Landau levels and absorb sonic energy. For metals and for sonic frequencies well below the electron plasma frequency, which is typically the order of 10^{16} Hz for metals, the electrons follow the motion of the ion cores closely so the induced electric field is weak. It is not expected then that the interaction of the conduction electrons with the induced electric field of longitudinally polarized sound will be the dominant interaction for DSACR in indium.

It is expected that for longitudinal sound the deformation of the Fermi surface is the dominant source of interaction. As the sonic wave travels through the crystal, there is a periodic deformation of the Fermi surface. An electron experiences deformation of the Fermi surface with a frequency ω_{eff} defined by Equation (9). The magnitude of the deformation is dependent on the "deformation potentials" for the Fermi surface. The deformation corresponds to a change in the cyclotron mass, m_c , which occurs with a frequency ω_{eff} . The cyclotron motion of the electrons is perturbed [Equation (24)] and there is a periodic change in energy of the Landau levels.

For absorption of energy from the sonic pulse by reason of either type of perturbation, the condition of Equation (23) must be met. For any value of R on the Fermi surface, there is an appropriate value of magnetic field, H , for which absorption can occur. A peak in the absorption is expected when a large number of electrons have the same value of R and satisfy Equation (23). The location of the peaks in H determines the value of R for these electrons through Equation (23).

Figure 2 shows a plot of R vs k_z for a hypothetical Fermi surface. R is nearly constant over a comparatively large range of k_z between $k_z^{(2)}$ and $k_z^{(3)}$. Since a large area of the Fermi surface and, hence, a large number of electrons have nearly the same value of R , an absorption peak is expected. It has been found experimentally that the amplitude of these absorption peaks is small compared to the type that occurs when $\partial R / \partial k_z$ equals zero. Absorption peaks of the former type were not observed in this investigation.

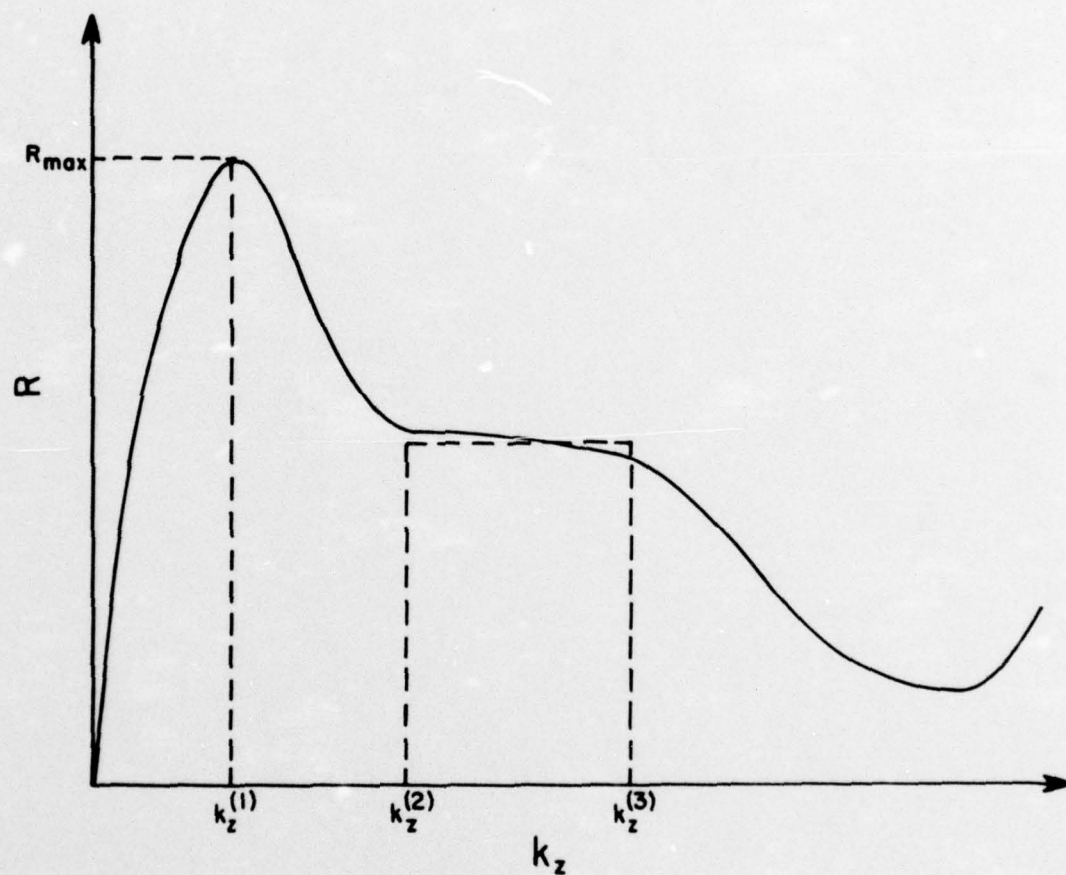


Figure 2. A plot of R vs. k_z for a hypothetical Fermi surface.

The absorption peaks observed arise because $\partial A(k_z)/\partial k_z$ has an extremal value. This corresponds to $k_z = k_z^{(1)}$ in Figure 2. It can be shown that in a narrow range Δk_z , a large number of cyclotron orbits lie on the Fermi surface compared to the number in the same Δk_z at non-extremal points.

For the cyclotron period we have

$$T = \frac{2\pi}{\omega_c} = \oint_C dt, \quad (29)$$

where the integral is taken around the cyclotron orbit. Using the Lorentz force equation [Equation (14)]

$$dt = \frac{\hbar}{eHv_n} dk_t, \quad (30)$$

where v_n is the component of the electron velocity normal to \vec{H} , and dk_t is the direction tangential to the cyclotron orbit in \vec{k} -space in the plane $k_z = \text{constant}$.

Then from Equations (29) and (30),

$$\omega_c = \frac{2\pi eH}{\hbar} \left(\oint_C \frac{dk_t}{v_n} \right)^{-1}. \quad (31)$$

Consider two cyclotron orbits on the Fermi surface separated by Δk_z and having cyclotron energies ϵ and $\epsilon + \Delta\epsilon$ corresponding to orbits at k_z and $(k_z + \Delta k_z)$, respectively, where $k_z = \text{a constant}$. Since

$$\vec{v} = \frac{1}{\hbar} \vec{\nabla}_k \epsilon, \quad (32)$$

for small $\Delta\epsilon$,

$$v_n = \frac{1}{\hbar} \frac{\Delta \epsilon}{\Delta k_n} \quad (33)$$

or

$$\Delta k_n = \frac{\Delta \epsilon}{\hbar v_n} \quad (34)$$

The difference in area enclosed by the two orbits, ΔA , given by Equation (19), is

$$\Delta A = \oint_C \Delta k_n dk_t, \quad (35)$$

where the integral is taken around the orbit in the $k_z = \text{a constant}$ plane. Then, using Equations (31), (34) and (35),

$$\Delta A = \frac{2\pi eH}{c\hbar^2 \omega_c} \Delta \epsilon \quad (36)$$

Let N_c be the number of cyclotron orbits that lie on the Fermi surface between k_z and $(k_z + \Delta k_z)$. Since $\hbar \omega_c$ is the energy difference between adjacent orbits,

$$N_c = \frac{|\Delta \epsilon|}{\hbar \omega_c} \quad (37)$$

Using Equation (36),

$$|\Delta \epsilon| = \frac{c\hbar^2 \omega_c}{2\pi eH} |\Delta A| = \frac{c\hbar^2 \omega_c}{2\pi eH} \left| \frac{\partial A(k_z)}{\partial k_z} \right| \Delta k_z \quad (38)$$

so that

$$N_c = \frac{c\hbar}{2\pi eH} \left| \frac{\partial A(k_z)}{\partial k_z} \right| \Delta k_z \quad (39)$$

For a fixed Δk_z , the number of cyclotron orbits on the Fermi surface in the range Δk_z is a maximum when $|\partial A(k_z)/\partial k_z|$ is maximum for which $\partial^2 A(k_z)/\partial k_z^2 = 0$. This corresponds to a maximum value of R [Equation (22)] symbolized by R_{\max} . Eckstein has shown that this type of absorption peak is "sharp" and has a Lorentzian line shape.⁷

The expected dependence of the sonic absorption, α , on $1/H$ is shown in Figure 3. The values of n correspond to those in Equation (23). $\Delta(1/H)$, the difference between values of $1/H$ for successive absorption peaks, is a constant. From this value of $\Delta(1/H)$, R_{\max} may be determined. In general, there are more than a single series of absorption peaks, each corresponding to a different value of R_{\max} .

Other conditions for observing DSACR absorption are apparent in the general theory but cannot be deduced from the physical picture presented here. It has been shown that the product $q\ell$ must be greater than one where ℓ is the electron mean-free-path.⁸ This condition is a statement of the fact that the electron must stay in phase with the sonic wave long enough to absorb a phonon before scattering. It has also been shown that when \vec{H} and \vec{q} are parallel to a crystal direction of s -fold symmetry, n in Equation (23) is replaced by sv , where $v = 1, 2, 3, \dots$.⁹ Hence, only absorption peaks for which $n = sv$ will be observed when \vec{q} and \vec{H} are parallel to a crystal axis of s -fold symmetry.

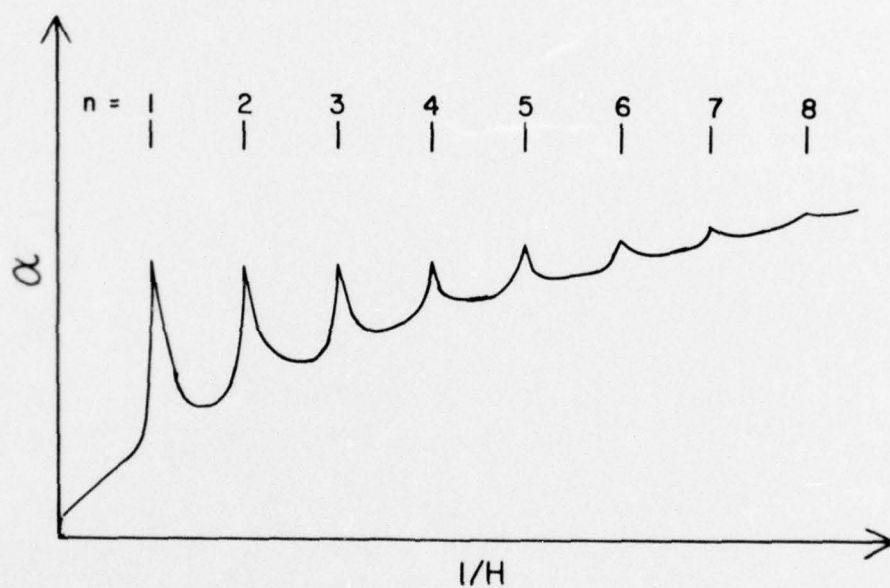


Figure 3. A plot of the sonic attenuation, α , vs. $1/H$ showing the behavior expected from the theory.

CHAPTER III

EXPERIMENTAL APPARATUS AND TECHNIQUES

Method Employed for Measuring Ultrasonic Attenuation in the Presence of a Magnetic Field

The pulse-echo technique was employed for measuring the attenuation of longitudinal sound in the presence of a varying magnetic field. RF pulses of about 1 μ sec duration was applied to a quartz or lithium-niobate transducer bonded to the specimen. A single ended system was used in which the same transducer served to convert an RF pulse into a sonic pulse and sonic echoes to an RF signal. Echoes corresponded to successive round trips through the specimen of the pulse which was reflected at opposite faces of the specimen. The signal sent to the receiving circuit consisted of a train of echoes decreasing in amplitude exponentially.

With specimens about 2 mm thick, the echoes were large enough in amplitude for reliable measurement. However, with a specimen this thin, the first echo arrives back at the transducer before the driving pulse is extinguished and successive echoes follow too close to be resolved. This was overcome by bonding a quartz delay rod 1 cm long to the parallel face of the specimen opposite the transducer. At liquid He temperatures the attenuation of sound in quartz is very small compared with In and is independent of magnetic field so that the resonances observed were due to the In.

The bonded faces of the specimen met necessary critical requirements. They were smooth compared to the sonic wavelength to minimize

scattering of the sound at the surface and they were flat and parallel to better than a wavelength of sound to minimize distortion in the echoes and conversion of longitudinal to transverse sound.

Apparatus for Measuring Doppler-Shifted Acoustic Cyclotron Resonance

There were three basic parts to the apparatus. They were the superconducting magnet, the liquid helium cryostat and the electronics for measuring the ultrasonic attenuation.

The superconducting magnet has already been described.¹⁰ It is a Varian Associates Nb-Ti alloy superconducting magnet variable from 0 to 50 kOe. It was used with a programmable Model V-4102 power supply. The magnet current was determined by measuring the potential difference across a precision 1 milliohm resistor in series with the magnet solenoid with a Hewlett-Packard Model 740B differential voltmeter. The magnetic field was calibrated against magnet current using a rotating-coil Rawson Electrical Instrument Co. Model 820 gaussometer. A least-mean-squares fit was then used to determine α and β in the relation $H(\text{kOe}) = \alpha I(\text{amperes}) + \beta$ for sweeps from low to high fields. Their values for magnetic fields from 0.4 to 50 kOe were:

$$\alpha = (2.7702 \pm 0.0005) \text{ kOe/amp} \quad (1)$$

and

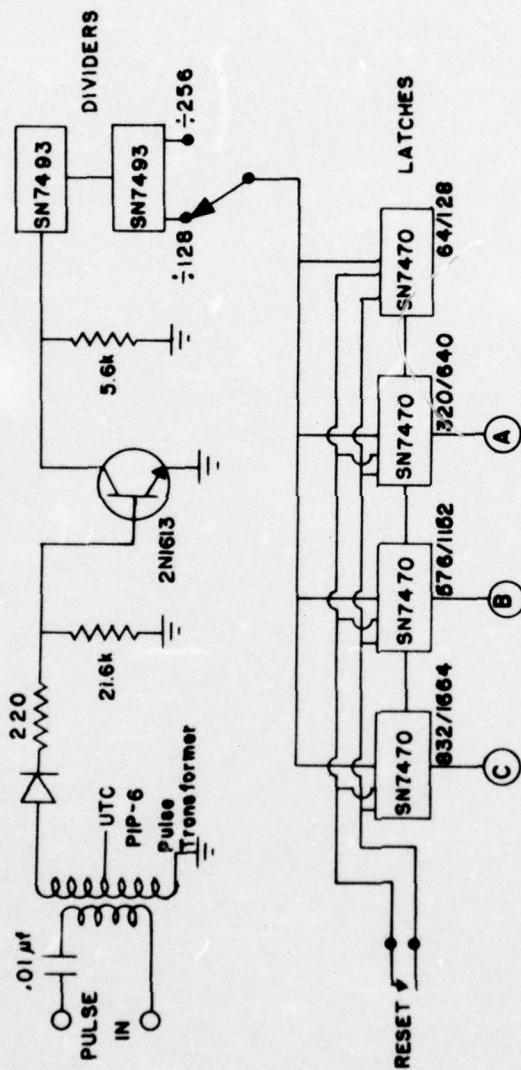
$$\beta = (-0.123 \pm 0.005) \text{ kOe} \quad (2)$$

The persistent current switches which were provided with the magnet were removed so that H was linearly dependent on I when sweeping the magnetic field.

Since the range in $1/H$ in which the data were recorded was large ($\sim 2.5 \times 10^{-3} \text{ kOe}^{-1}$) it was not feasible to use the $1/H$ sweep control to drive the magnet power supply. However, a large number of data points were needed for sufficient resolution of sonic absorption data in the region of small magnetic fields when using a linear sweep. The problem was solved by using the multi-ramp sweep unit shown in Figure 4.¹⁰ The unit consists of a digital counter with latched output (Figure 4a) which drives a programmable integrator (Figure 4b). With the dividers set on divide-by-128, they change state (open or close) after every 128 input pulses. The output of the dividers is used to automatically close the four latches (switches) in succession, for divide-by-128, after 64, 320, 576, and 832 input pulses. The output of the latches (A, B, and C in Figure 4a) is a step function which drives the integrator changing dV/dt whenever a latch is closed. The four values of dV/dt are set with the gain adjust (Figure 4b). The voltage ramps are input to the magnet power supply which is a V-to-I converter. In the fast mode and on divide-by-128, this provided four linear sweep rates starting at the low field end of 320 counts at 4.8 milliamps/sec and then 256 counts at 6.3 milliamps/sec, 9.5 milliamps/sec, and 16.8 milliamps/sec.

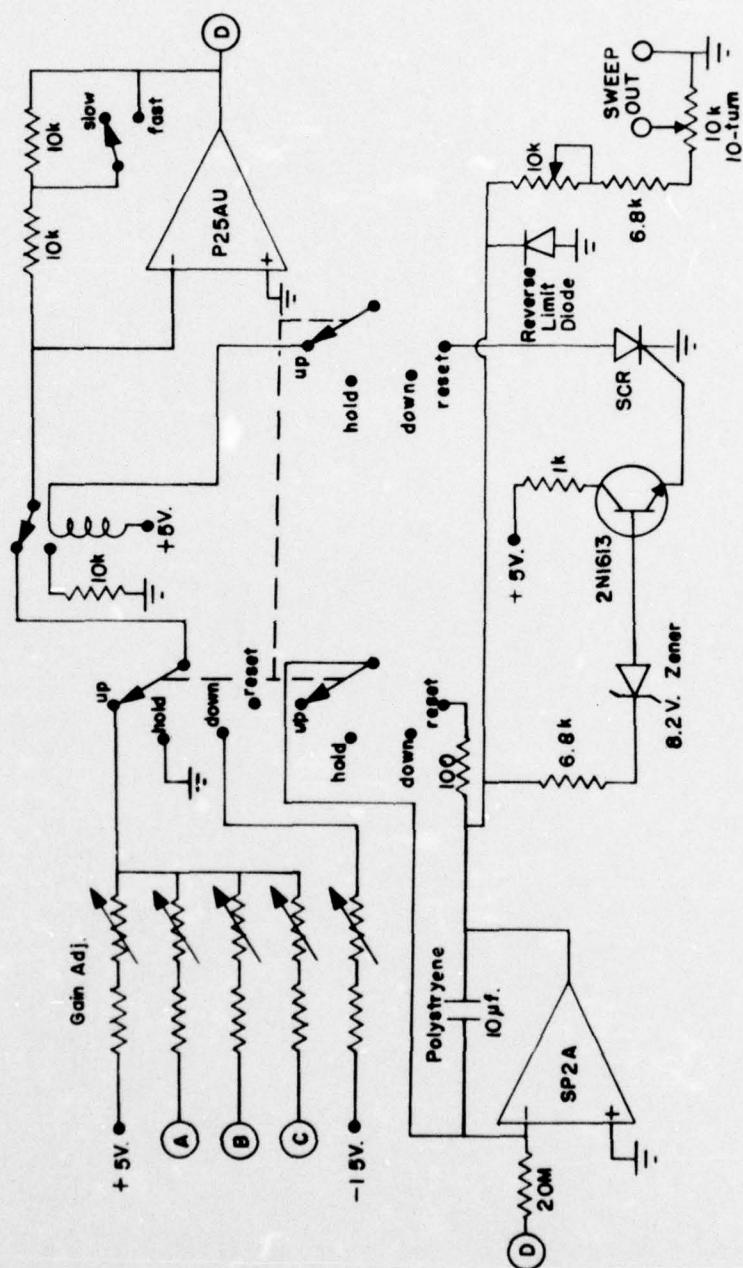
The rotating specimen holder and finger dewar are described in reference 10. The specimen holder was rotatable in a plane containing \vec{q} and \vec{H} with the angle between \vec{q} and \vec{H} variable from -30° to $+90^\circ$.

Low temperatures were achieved by pumping on the He bath in a finger dewar in the core of the superconducting magnet with an Edwards High Vacuum Ltd. Model 9133 vapor booster pump yielding a minimum



a. Digital counter with latched output.

Figure 4. Multi-ramp sweep unit used to provide the ramp to the magnet power supply.



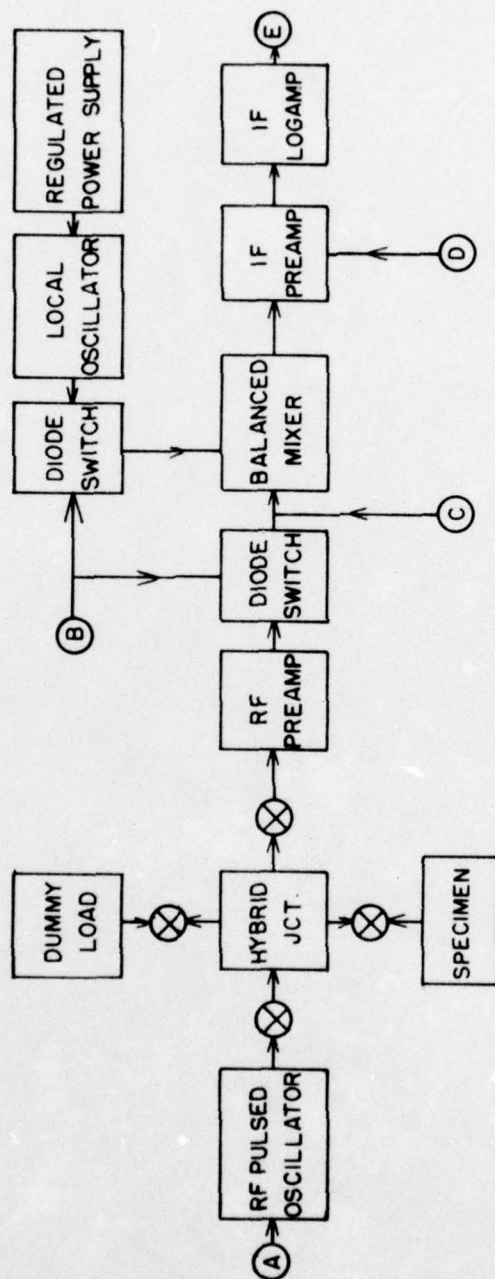
b. Programmable integrator.

Figure 4 (cont.)

pressure over the liquid-He bath of ≤ 0.1 mmHg. Intermediate pressures up to 1 atm. were achieved using a manostat regulator in the vacuum line allowing data to be taken in a temperature range from 4.2 K down to 1 K.

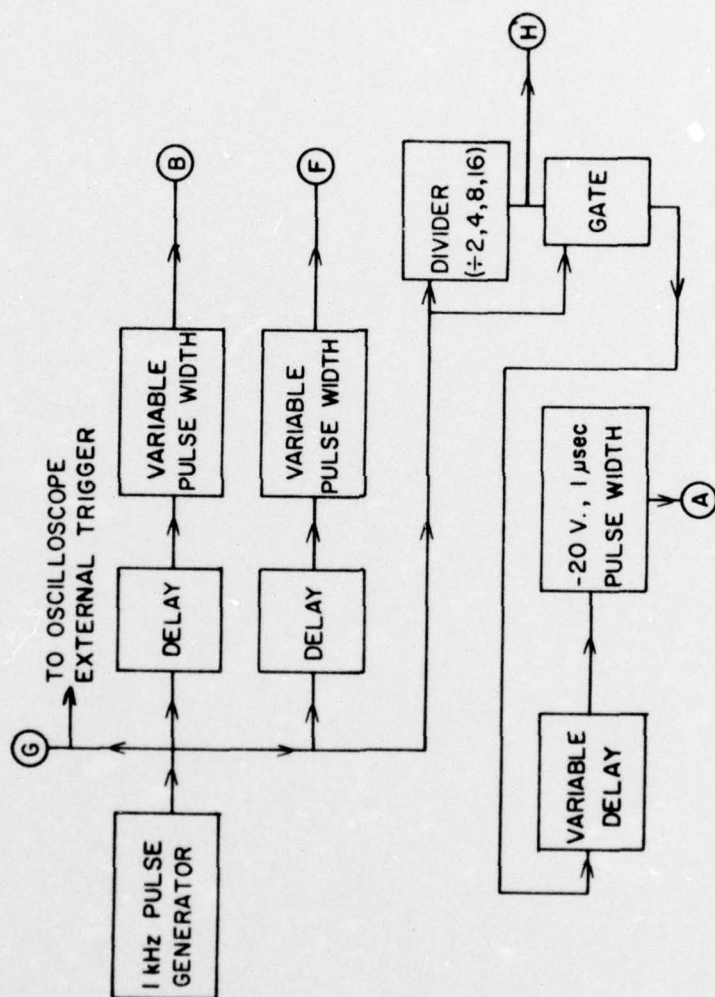
A block diagram of the electronic apparatus is shown in Figure 5. It consisted of four basic sections. The acoustical signal (Figure 5a) and automatic gain control (Figure 5b) sections are described elsewhere.¹² Two RF pulsed oscillators were used depending on the sonic frequency desired. A range of 20 to 180 MHz with a peak power of 400 watts was provided by an Arenberg Ultrasonic Laboratory Model PG 650C and of 200 to 500 MHz with a peak power of 2.5 kwatts by an American Microwave Laboratories, Inc. Model 1223. Both oscillators generated 1 μ sec pulses with a repetition rate of 500 Hz when using "divide-by-two" in the trigger-chop divider in the timing section (Figure 5c). The RF preamplifier greatly improved the signal-to-noise ratio; however, it could not be tuned below 200 MHz. The signal-to-noise ratio in the low frequency range was satisfactory without the RF preamplifier. The receiver is of a superheterodyne type with an intermediate frequency (IF) of 30 MHz. The logarithmic amplifier was used to provide a video detected output proportional to the logarithm of the IF signal input which served to eliminate scale changes when recording both large and small amplitude resonances in addition to providing a linear dB calibration for attenuation changes.

The timing section (Figure 5c) provided the triggers and reference signals to the various electronic components. The "master" timing signal used to generate the triggers and reference signals was provided



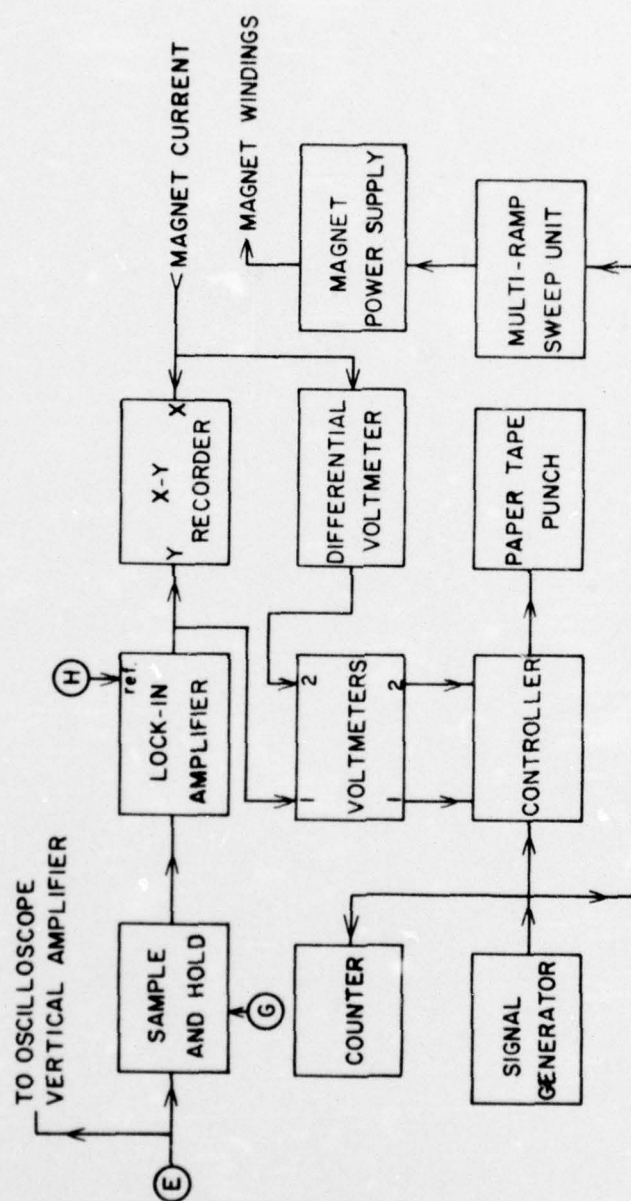
a. Acoustic signal section.

Figure 5. Block diagram of the electronic part of the apparatus used to measure the ultrasonic attenuation.



c. Timing section.

Figure 5 (cont.)



d. Recording section.

Figure 5 (cont.)

by the 1 kHz pulse generator. A negative 20 volt chopped trigger with a width of 1 μ sec was provided for the RF pulsed oscillator in Figure 5a. The repetition rate of the chopped trigger equals the value of the "divide-by" setting on the divider divided into 1 kHz. A square wave reference signal synchronized with the chopped trigger is provided for the lock-in amplifier (Figure 5d). Triggers at a repetition rate of 1 kHz are also provided for the high-speed sample and hold and the diode switches.

The recording section is shown in Figure 5d. The recording of signals only slightly greater than the noise level was possible with the use of the high-speed sample and hold circuit shown in Figure 6 and a lock-in amplifier. The high-speed sample and hold circuit sample time was set at 400 nanosec with the gate width control in Figure 6. The echo to be sampled was selected by adjusting the delay control ahead of the gatewidth circuit used in conjunction with the actual sample and hold circuit shown on the lower half of Figure 6. The signal level to be held could be changed at the rate of ± 40 v/ μ sec. The lock-in amplifier was a Keithley 840 Autoloc Amplifier. The reference signal to the lock-in amplifier, supplied by the timing section, is a square wave synchronized with the RF pulsed oscillator and its frequency matched the output frequency of the sample and hold circuit. For example, using the 1 kHz repetition rate and divide-by-two set on the divider in Figure 5c, the sample and hold circuit samples every millisecond. However, a chopped trigger to the RF pulsed oscillator is supplied every 2 milliseconds and the reference signal to the lock-in is a 500 Hz square wave. In this situation the

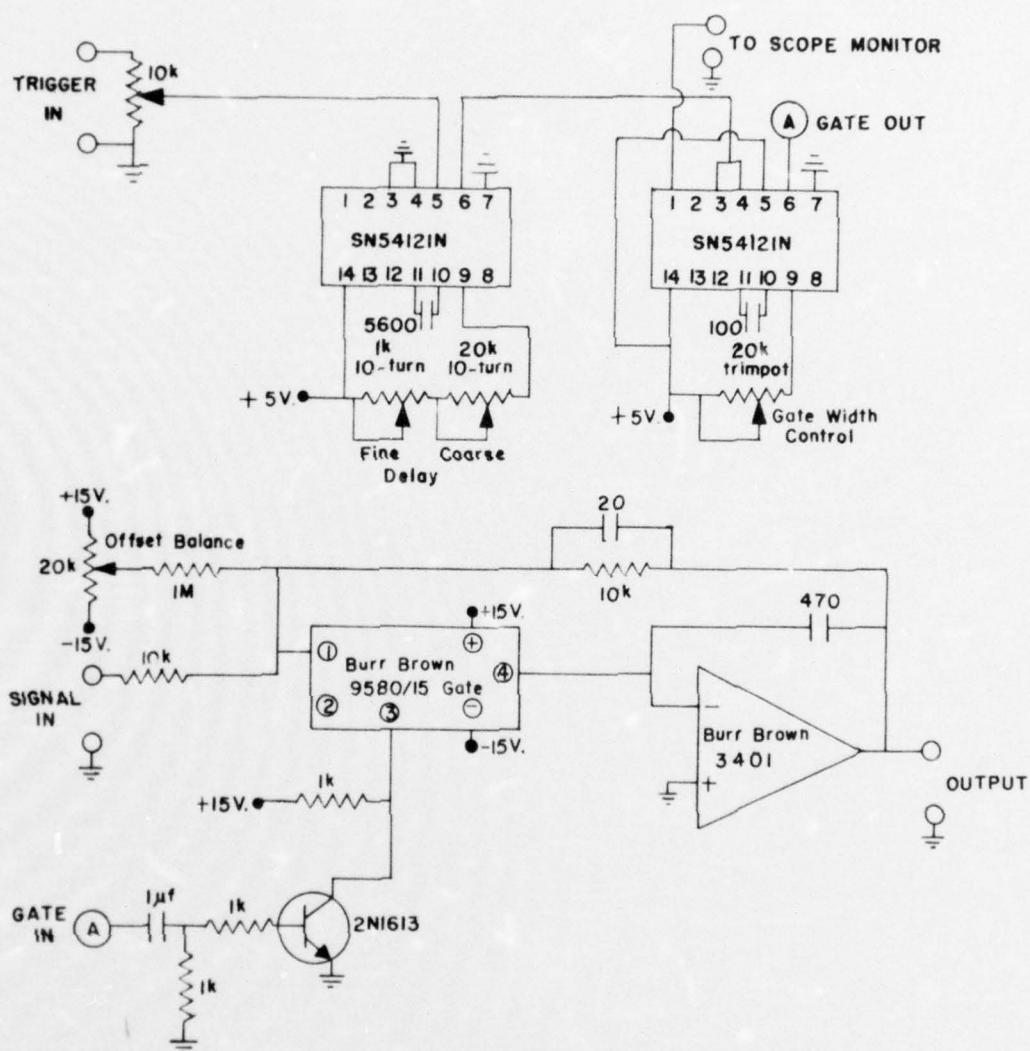


Figure 6. High-speed sample and hold circuit with variable gate and delayed trigger.

sample and hold circuit samples the signal plus noise and holds for 1 millisecond after which it samples and holds the noise for 1 millisecond. The result is a 500 Hz square wave with its minimum voltage equal to the video detected noise voltage above ground and a maximum voltage equal to the noise plus signal above ground. Thus, the output of the lock-in is the D.C. signal level with the noise averaged out. This was recorded as the ordinate on an X-Y recorder and punched in four digit code on the first channel of the paper tape punch. The voltage drop across the milliohm resistor in series with the magnet windings, which is proportional to magnet current and, hence, magnetic field, is recorded as the abscissa on the X-Y recorder and, after amplification by the differential voltmeter, is recorded on channel two of the paper tape punch. A Digitec paper tape punch and controller was used. The X-Y recorder was a Moseley Model 7001 AM and the differential voltmeter a Hewlett-Packard Model 740B. The timing signal for the paper tape punch and the multi-ramp sweep unit is provided by a Krohn-Hite signal generator Model 440AR. The number of counts is registered on a Hickok Model 0P150 LMC counter.

Specimen Preparation

A single crystal rod of indium about 1.3 cm in diameter and 12 cm long was purchased from Research Crystals, Inc., Orangeburg, New York. The single crystal had been grown by the Czochralski technique from starting material 99.9999% pure. The residual resistivity ratio, $\rho(300K)/\rho(4.2K)$, was 8950 ± 450 which was measured using the eddy current decay method.¹³ Although the chemical purity was high, diffuseness of the Laue X-ray spots gave evidence of more than normal

strain in the specimens. Because indium is a very soft material, additional strain was introduced in the preparation of specimens from the single crystal rod. To minimize this strain, a spark-erosion method, which is non-abrasive, was used to cut and plane the specimens. This method has the advantage that a machining tool never touches the specimen. The cutting or planing is accomplished in a kerosene bath by a spark jumping from the machining tool to the specimen.

In the preparation for cutting a specimen, the single crystal rod was cemented on a copper trough to support the weight of the rod along its axis. Duco cement was used since it is soluble in acetone permitting the specimen to be removed without damage. A General Electric XRD-5 X-ray machine with a tungsten target X-ray tube was used to orientate the single crystal rod to within 10° of a desired crystalline direction by the Laue-back-reflected diffraction method. Once orientated, conducting silver paint was applied to insure good electrical contact between the rod and the copper trough.

A Metals Research, Ltd., Servomet SMD spark erosion machine with a wire slicer attachment was used to cut a disc from the single crystal rod. The wire slicer attachment uses as a cutting tool a 0.46 mm diameter tinned copper wire which is continuously pulled across the rod. Using only the lowest sparking power ranges, the time required to make one cut was about six hours. A disc was cut with a thickness about twice the desired thickness of the finished specimen.

The disc was cemented to a two-circle goniometer and orientated to within 1° of the desired crystalline direction. Discs cut at large angles with the axis of the rod were trepanned to 1 cm diameter to fit

in the specimen holder. A planing wheel replaced the wire slicer (or trepanning tool) on the Servomet and one surface of the disc was planed flat using only the lowest sparking power range.

To insure that the opposite face is planed parallel to the first face planed, a piece of aluminum block was planed flat and the previously planed face was placed on it. Cement and silver paint were applied only around the edges of the disc and not between the face of the disc and the aluminum block. The opposite face was then planed flat.

Using only the lowest sparking power range and working with caution, the planed surfaces exhibited damage as evidenced by the diffuseness of the Laue spots. Much of the damage was removed as evidenced by the improvement in the Laue spots by etching each face for 30 seconds in a solution of equal parts of concentrated HNO_3 and H_2O . Further etching rounded the flat surface to a point where a bonding of the transducer was not reliable.

Some specimens were annealed at 120°C for approximately 24 hours. They showed only a small improvement in the sharpness of the Laue spots. Annealing rounded the flat surface and made an acoustic bond unreliable. Accordingly, specimens used in this investigation were not annealed.

Specimens prepared in the above manner were oriented so that the sonic wave number, \vec{q} , was parallel to the $[001]$, $[100]$, or $[110]$ directions of the face-centered tetragonal structure. The specimens were approximately 1 cm in diameter and 2 mm thick with flat and parallel faces perpendicular to the direction of the sound propagation.

Specimen Bonding

A 20 or 25 MHz transducer and a z-cut quartz delay block were bonded to the specimens. Both x-cut quartz and lithium-niobate transducers were used to generate longitudinal sonic waves. The lithium-niobate transducers were only slightly more effective than the quartz transducers. The transducers were 0.945 cm in diameter and the quartz delay block was 0.945 cm in diameter and 1 cm long. The bonding agent was a low-temperature epoxy made by mixing ten parts of Hysol Type R9-2039 resin to three parts Hysol Type H2-3561 hardener. General Electric "Clear-Seal" silicon rubber adhesive was also used as a bonding agent. Since the difference in the coefficients of thermal contraction between the indium and silicon rubber adhesive is smaller than between the indium and the epoxy, the strain applied to the indium when the specimen is cooled to liquid-He temperatures was smaller for the silicon rubber adhesive bonds. However, the epoxy bonds were more reliable. Dow Corning 200 fluid, having a viscosity of 60,000 centistokes at 25°C, was also tried as a bonding agent. Acoustic coupling was lost at liquid nitrogen temperatures, however, so it was not used in this investigation.

When the bond had cured, the specimen with the attached transducer and delay block was placed in the specimen holder. Laue backscatter patterns were taken on the edge of the specimen in order to be able to rotate the specimen in its holder about a desired crystal axis.

An acoustic signal was observed at room temperature and then the specimen and its holder were cooled to liquid nitrogen temperature before emersion into the liquid-He cryostat in preparation for taking data.

CHAPTER IV

MODEL OF INDIUM FERMI SURFACE

Indium has 49 electrons in a $1s^2 2s^2 2p^6 3s^2 3p^6 3d^{10} 4s^2 4p^6 4d^{10} 5s^2 5p$ configuration. In the solid state In has 3 conduction electrons, the $5s^2$ and $5p$ electrons.

The crystal structure of In is face-centered tetragonal with lattice constants $a = 4.5557\text{\AA}$ and $c/a = 1.0831$ at 4.2 K.¹⁴ Figure 7 shows the first Brillouin zone of In where the \vec{G}_i are the reciprocal lattice vectors. $|\vec{G}_1| = 0.923$ and $|\vec{G}_2| = |\vec{G}_3| = 1.000$ in units of $2\pi/a$. The free-electron Fermi surface constructed by the method described by Harrison in a reduced zone scheme is shown in Figure 8.¹⁵ The conduction electron states of the first Brillouin zone are completely filled. The Fermi surface in the second zone, Figure 8a, is a hole surface multiply connected at W. The Fermi surface in the third zone, Figure 8b, is an electron surface which consists of a ring of four connected β -arms and eight α -arms connected to the junctions of the α -arms. Small electron pockets are also predicted in the fourth zone, but are not shown.

Measurements of the high-frequency magnetoacoustic effect,¹⁶ radio-frequency size effect,¹⁷ cyclotron resonance cutoff,¹⁸ the cyclotron mass using the cyclotron resonance method,¹⁹ and de Haas-van Alphen effect²⁰ are all in essential agreement with the free-electron model of the second-zone surface. However, the agreement with the free-electron model of the third-zone electron surface is not

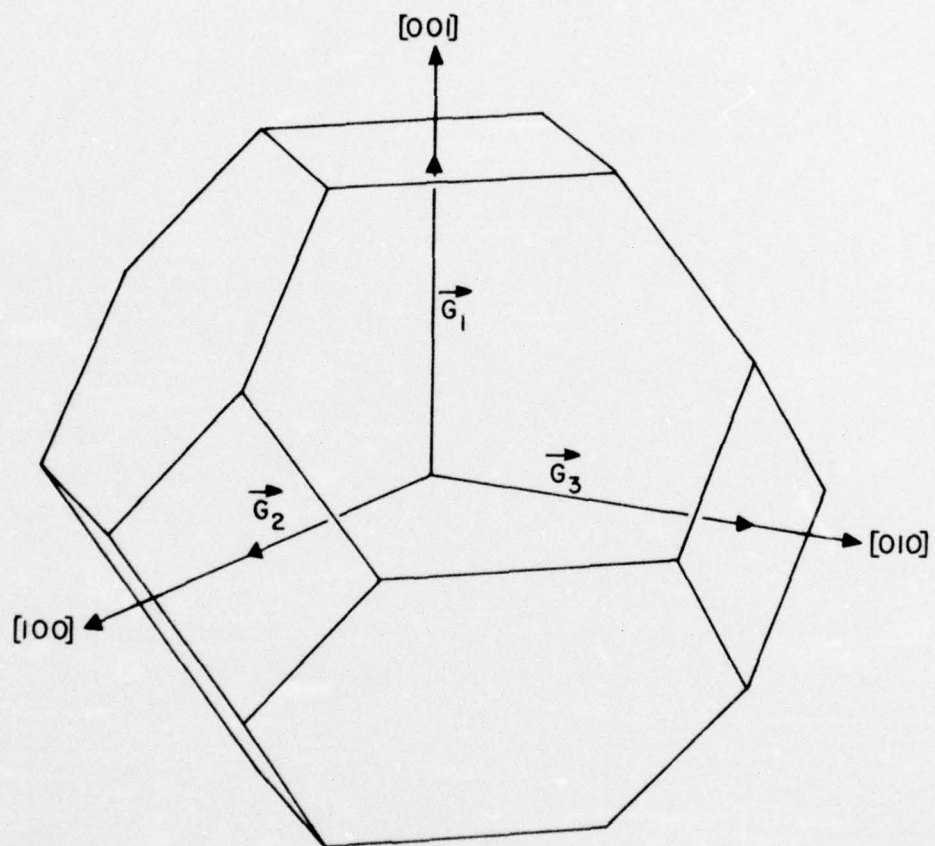
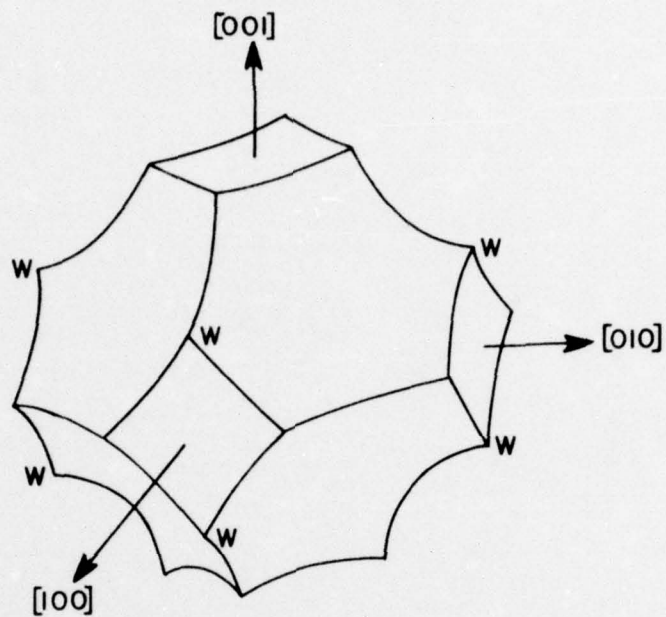
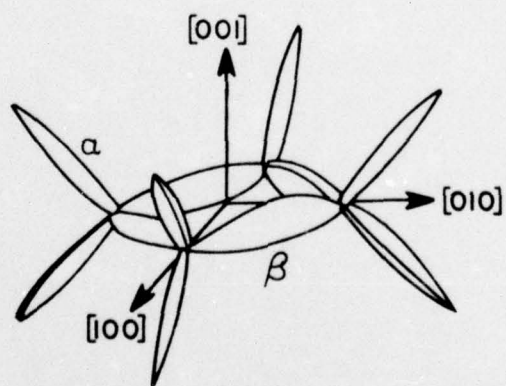


Figure 7. The first Brillouin zone of indium.



(a)



(b)

Figure 8. The free-electron model of the Fermi surface of indium.

good. De Haas-van Alphen²¹ and high-frequency magnetoacoustic²² measurements indicate that the extremal area of cross section of the β -arms along the $[110]$ direction is smaller by a factor of 1.8 than the free-electron prediction. In the case of the de Haas-van Alphen measurements, the extremal area of cross section of the α -arms along the $[011]$ direction is larger by a factor of 1.6. If true, this means that the extremal areas of cross section of the α - and β -arms in planes normal to their respective axes are very nearly equal. Other measurements reported do not exhibit any evidence of the α -arms. O'Sullivan, Schriber and Anderson (OSA) have calculated the Fourier components of an effective potential using a local pseudopotential in a 6-OPW approximation by fitting the extremal areas of the β -arms in reference 21.²³ The extremal areas of the second zone calculated with this pseudopotential are in slightly better agreement with the experimental data than the free-electron values. This pseudopotential model predicts that the second zone corners of the free-electron model are rounded instead of pointed. It eliminates the fourth zone electron pockets and removes the multiple connections of the free-electron second-zone surface at the corners labeled W in Figure 8. The rounding of the corners of the second-zone surface and the elimination of the multiple connections at W seem to be in agreement with experimental results.

The values of R_{\max} defined by Equation (22) in Chapter II, have been calculated for the second zone using the OSA model and are displayed in Figure 9.²⁴ Measurements of the values of R_{\max} using the Sondheimer size effect are in essential agreement with these

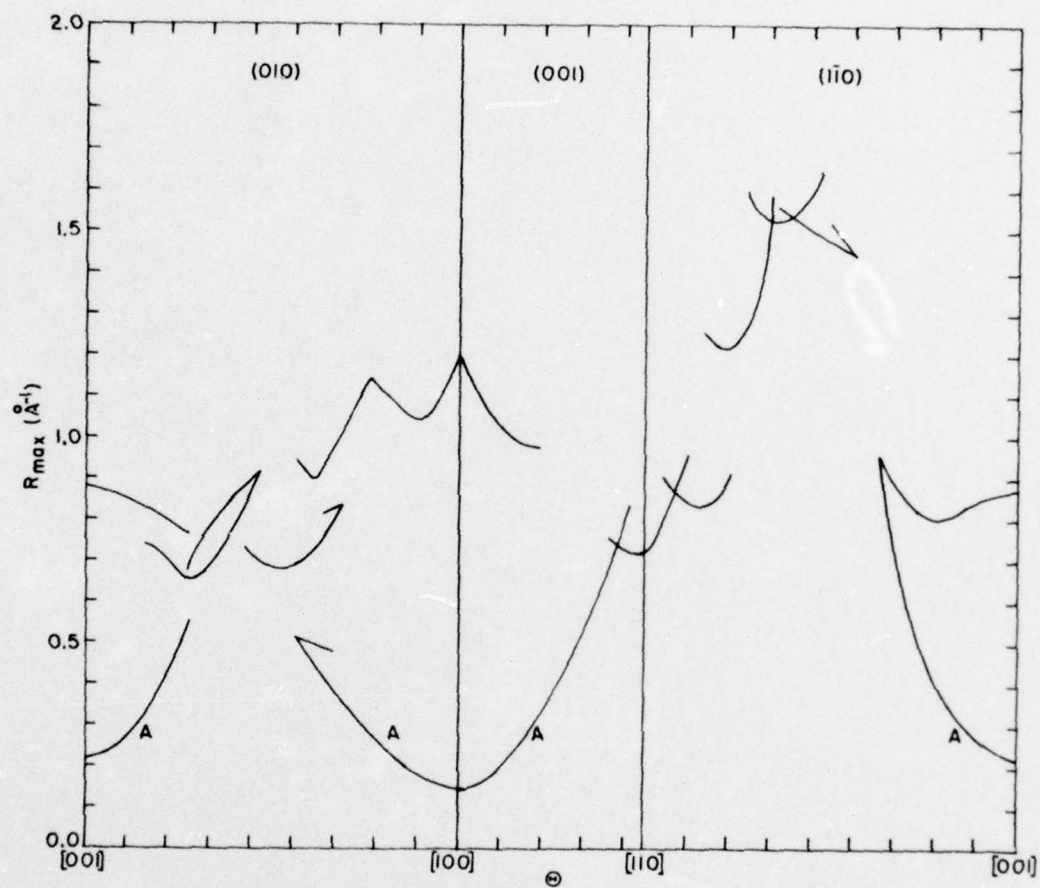


Figure 9. R_{\max} on the second-zone hole surface of indium calculated using the OSA model.

calculations except for the curves labeled A for which no values were observed.²⁵

Fitting existing β -arm data, local pseudopotential calculations have also been made by Hughes and Shepherd (HS)²⁶ and Ashcroft and Lawrence (AL).²⁷ Neither the HS or AL models predict the existence of the α -arms. In the case of the HS model this is not surprising since in making the calculations it was assumed they did not exist. Ashcroft and Lawrence point out that the pseudopotential parameters will have a more pronounced effect on the α -arms than on the β -arms since the α -arms lie closer to the Brillouin zone boundaries.²⁸ They show that changes in the parameters which do not significantly affect the β -arm areas or the Fermi surface volume give different results for the α -arms. The combination of parameters under which the α -arms do exist is ruled out as a likely possibility by Ashcroft and Lawrence.

If it is supposed that the α -arms do not exist, it remains to explain the experimental evidence mentioned earlier. The experimental evidence of the existence of the α -arms in reference 21 was seen only for directions of magnetic field, \vec{H} , in the neighborhood of the [001] direction. Since indium is a soft material and hence, easily strained, it has been suggested that the observed de Haas-van Alphen oscillations attributed to α -arms were actually due to β -arms in a portion of the specimen which has become [100] due to recrystallization. Recrystallization is not uncommon in materials which have slip planes along which stresses may easily be relieved.²⁹ The fact that the observed extremal cross sections observed by Brandt and Rayne (reference 21) were equal for the α - and β -arms strengthens this argument.

It is also interesting to note that the In specimens used in the de Haas-van Alphen measurements were of 99.98% purity in order to avoid appreciable eddy currents which made measurements extremely difficult.³⁰ There is also strong evidence of the existence of the α -arms in the neighborhood of the [001] direction in some magnetoacoustic quantum oscillation measurements in indium doped to 0.01% at. wt. Sn.³¹ These measurements of the extremal cross-sectional areas agree with those of reference 30. However, using the same 99.9999% pure In specimens as used in this DSACR investigation, for an investigation of the magnetoacoustic quantum oscillations, no evidence for α -arms was observed. This seems to be in conflict with the recrystallization suggestion since the Laue photographs for the pure indium indicated more strain than the photographs for the indium with 0.01% Sn. Whether or not the α -arms exist appeared to be an open question when this research was undertaken.

Since there were no model calculations for R_{\max} in the third zone, a free-electron calculation was made for \vec{H} oriented in the (010) plane. Two computer programs, which along with all other computer programs used in this investigation are on file in the office of Professor F. G. Brickwedde, Osmond Laboratory, University Park, Pennsylvania, were written for the calculation of R_{\max} using The Pennsylvania State University's IBM Model 360 computer. The direction of \vec{H} was varied by intervals of 4° except within 10° of the [001] and [100] axes where the interval was 2° . For each orientation of \vec{H} the program GENCIR calculated the radii and the location of the origins and intersection points of the circles formed by the intersections of free-electron

Fermi spheres centered about the fourteen reciprocal lattice points nearest to the origin in reciprocal space with planes normal to the direction of \vec{H} . For each orientation of \vec{H} , the distance between adjacent planes used was 0.01 in units of $2\pi/a$. According to the method of Harrison (32), the cross sectional areas in each plane for the third-zone electron surface are those areas enclosed by three circles. Once these areas were identified by plotting the circles for each plane, program A3BRZN was used to calculate the area with the information provided by GENCIR. In addition to the area, A3BRZN also calculated $\partial A / \partial k_z$ where \vec{H} is in the \hat{k}_z -direction, by approximating each point and those adjacent to it on each side with a polynomial of degree two. That is, for the i^{th} value of k_z , the area, $A_i(k_z)$, is approximated by

$$A_i(k_z) \approx a_i k_z^2 + b_i k_z + c_i \quad (1)$$

where a_i , b_i , and c_i are calculated from the points $(A_{i-1}, k_{z_{i-1}})$, (A_i, k_{z_i}) , and $(A_{i+1}, k_{z_{i+1}})$. Then

$$\frac{\partial A_i(k_z)}{\partial k_z} \approx 2a_i k_z + b_i \quad (2)$$

The values of $|\partial A / \partial k_z|$ are then plotted as a function of k_z for each orientation of \vec{H} so that the values of $|\partial A / \partial k_z|_{\text{max}}$ and, hence, R_{max} can easily be identified. The results of this calculation are shown in Figure 10. It is not expected that experimental values of R_{max} will agree well with these calculated values of R_{max} for the third zone since it is known that the free-electron model is not a good

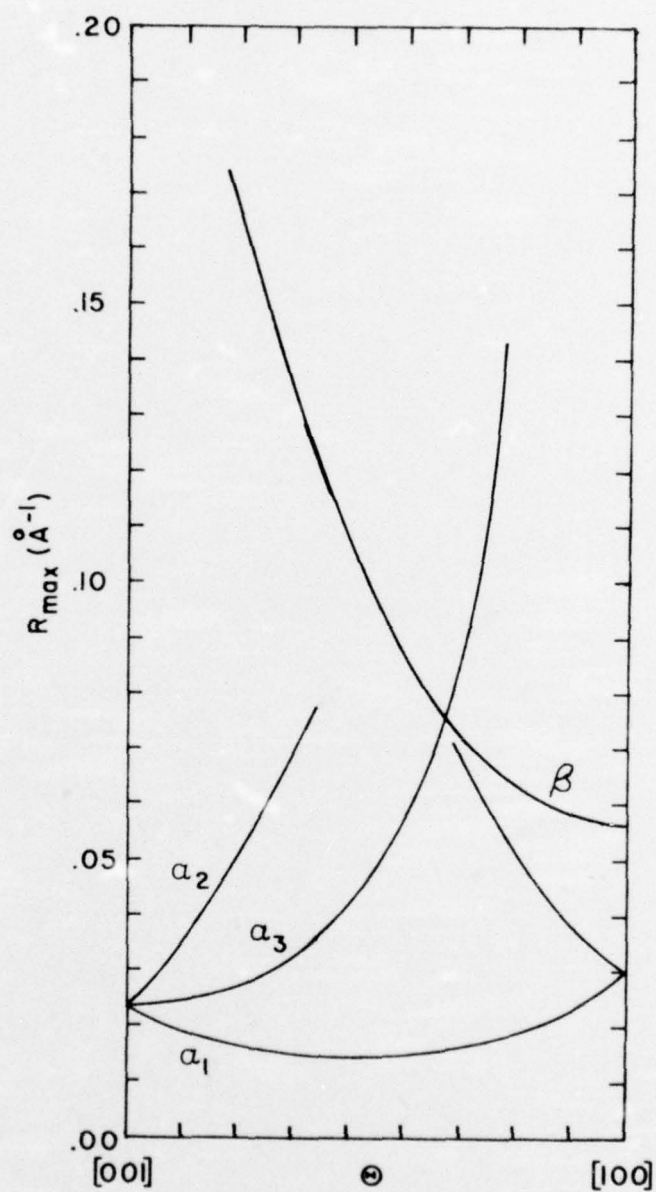


Figure 10. Calculated values of R_{\max} using the free-electron model in the third zone.

approximation for the third-zone Fermi surface. In addition, it was found that the magnitude of R_{\max} depended upon the sizes of the increment Δk_z between adjacent planes. However, Figure 10 is the best picture we have of the variation of R_{\max} as a function of the orientation of \vec{H} in the (010) plane.

CHAPTER V

EXPERIMENTAL RESULTS

The Data

The experimental data were obtained in the manner described in Chapter III. Three specimens, cut with different crystalline orientations from the same single crystal, were used. In each, the direction of the magnetic field was varied in two planes. For the specimen with \vec{q} parallel to $[001]$, \vec{H} was varied in the (010) and $(1\bar{1}0)$ planes. For the specimen with \vec{q} parallel to $[100]$, the variations of \vec{H} were in the (010) and (001) planes and for \vec{q} parallel to $[110]$, in the (001) and $(1\bar{1}0)$ planes. Data were recorded for the angle θ between \vec{q} and \vec{H} ranging in each plane from -12° to 80° in increments of 4° except around a principal crystal axis where the increments were 2° .

The experimental data were recorded by two means. First, as the magnetic field increased, the sonic echo-height was recorded continuously as a function of the magnet current, being related to it by Equations (1) and (2) in Chapter III. A typical plot from the X-Y recorder is shown in Figure 11. At the same time that data were being recorded with the X-Y recorder, the echo-height vs. magnet current data were also recorded automatically, at closely spaced intervals, on a punched paper tape. Information pertinent to each magnet sweep such as the direction of \vec{q} , rotation plane of \vec{H} , sonic frequency, angle between \vec{q} and \vec{H} , and temperature were manually punched into the first seven eight-digit words. The magnet current and echo-height were punched every second giving approximately 1000 points per sweep.

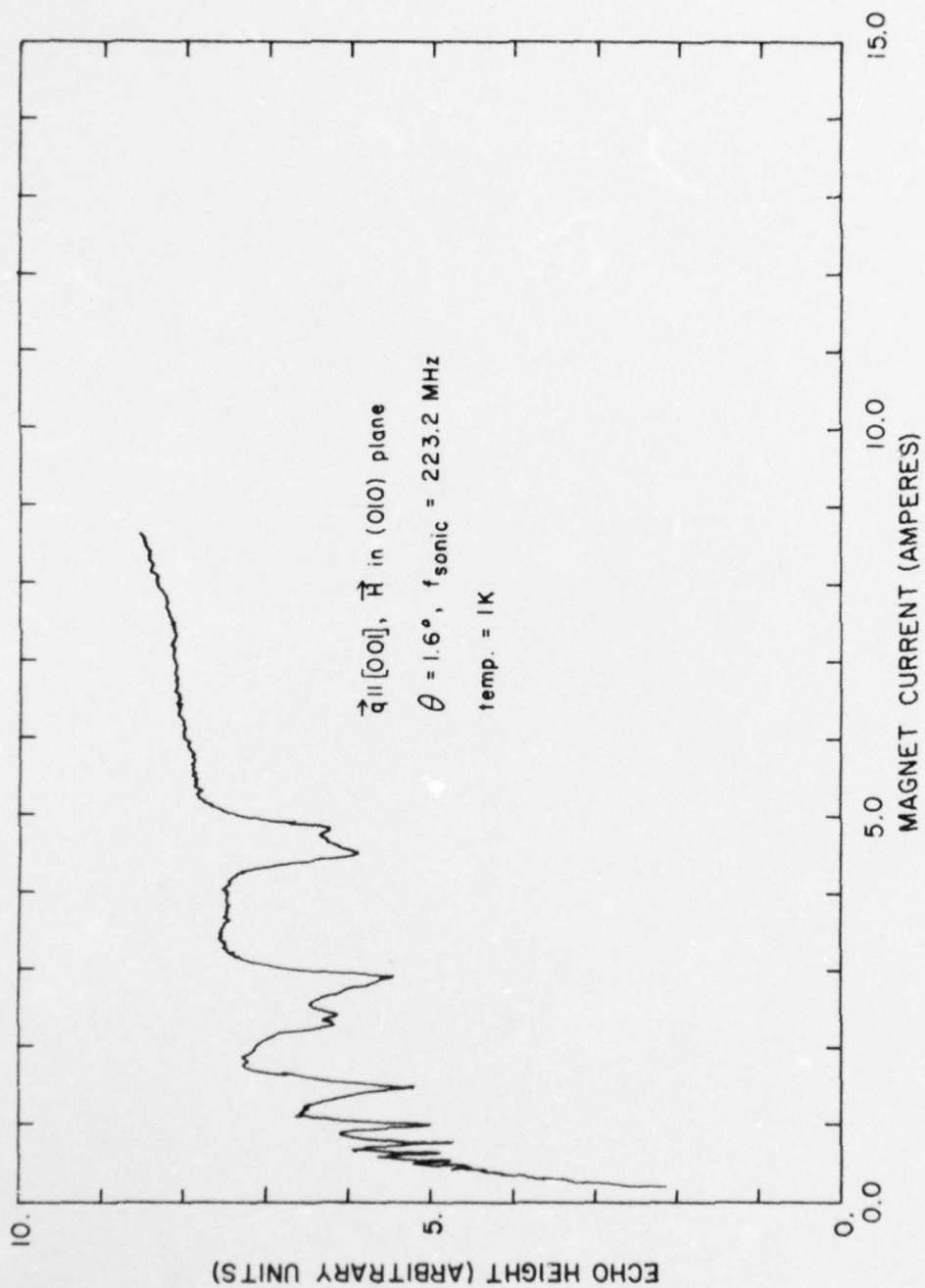


Figure 11. A plot of echo-height vs. magnet current from the X-Y recorder.

Analysis of the Data

The data recorded on the punched paper tape were transferred to magnetic tapes using a PSU-supplied program in preparation for computer analysis. The data on the magnetic tapes were processed by a computer program named DOPANY. DOPANY performed several functions. Since the paper tape punch code was not standard, the data on the magnetic tapes were translated to a form usable by the Penn State computer. As discussed in Chapter III, the data consisted of one, two, three, or four segments, each segment corresponding to a particular linear rate of sweep H ; i.e., magnet current. Since the resonances are periodic in $1/H$ (see Chapter II), the $1/H$ values were calculated for each punched data point and then the echo-height values interpolated to correspond to equal intervals in $1/H$ in preparation for a Fourier analysis (see Appendix B). In order to increase the resolution which is discussed in Appendix B, the values of H were extrapolated back from 400 gauss to 100 gauss before interpolation. A Fourier analysis was made for each sweep of the magnetic field. The sum of the Fourier coefficients (a_k and b_k in Appendix B) squared were plotted as a function of the period in $1/H$ in order to account for the phases ϕ (Appendix B) of the resonance absorption series. The determination of the period, $\Delta(1/H)$ of an oscillation in echo-height by this method was generally poor since the echo-heights were not sinusoidal functions of $1/H$ and there were usually less than ten periods in the recorded data.

DOPANY supplied, in the form of punched card output, values of echo-height and magnet current which have been translated to a usable form for each data point. These cards were used as the input for the

computer program GRAPIT. GRAPIT converted the echo-height data to attenuation relative to an arbitrarily set zero point in dB using the calibration for the logarithmic amplifier described in Chapter III and converted magnet current data to l/H data. GRAPIT then created as output the instructions for the PSU Calcomp Plotter using the PSU Quick Draw Graphics Subroutine Package for plotting the relative attenuation vs. l/H . Figure 12 is such a plot using the data displayed in Figure 11.

By handling the experimental data in this manner, series of resonances in the absorption were readily identified on the attenuation vs. l/H Calcomp plots. The three series, a, b, and c, shown in Figure 12, correspond to $\Delta(l/H) = 0.1235, 0.0807, \text{ and } 0.0755 \text{ (kG)}^{-1}$ respectively. These values were obtained by reading the l/H value for each n from the Calcomp plots and then calculating a least-mean-square value for the slope of a plot of l/H vs. n . Since the differences in l/H between adjacent points are small for small values of l/H (large H), the scaled value for n small is expected to be more precise. Hence, a weighting factor of $1/(n+1)^2$ was used in the least-mean-square fit. The values of R_{\max} , where R is defined by Equation (22) of Chapter II, were calculated using Equation (23) of Chapter II, for each series in l/H . The results of this kind of analysis of the data are shown in Figure 13 where the abscissa is θ , the angle between \vec{q} and \vec{H} . The values of R_{\max} along principal directions of crystal symmetry are given in Table I.

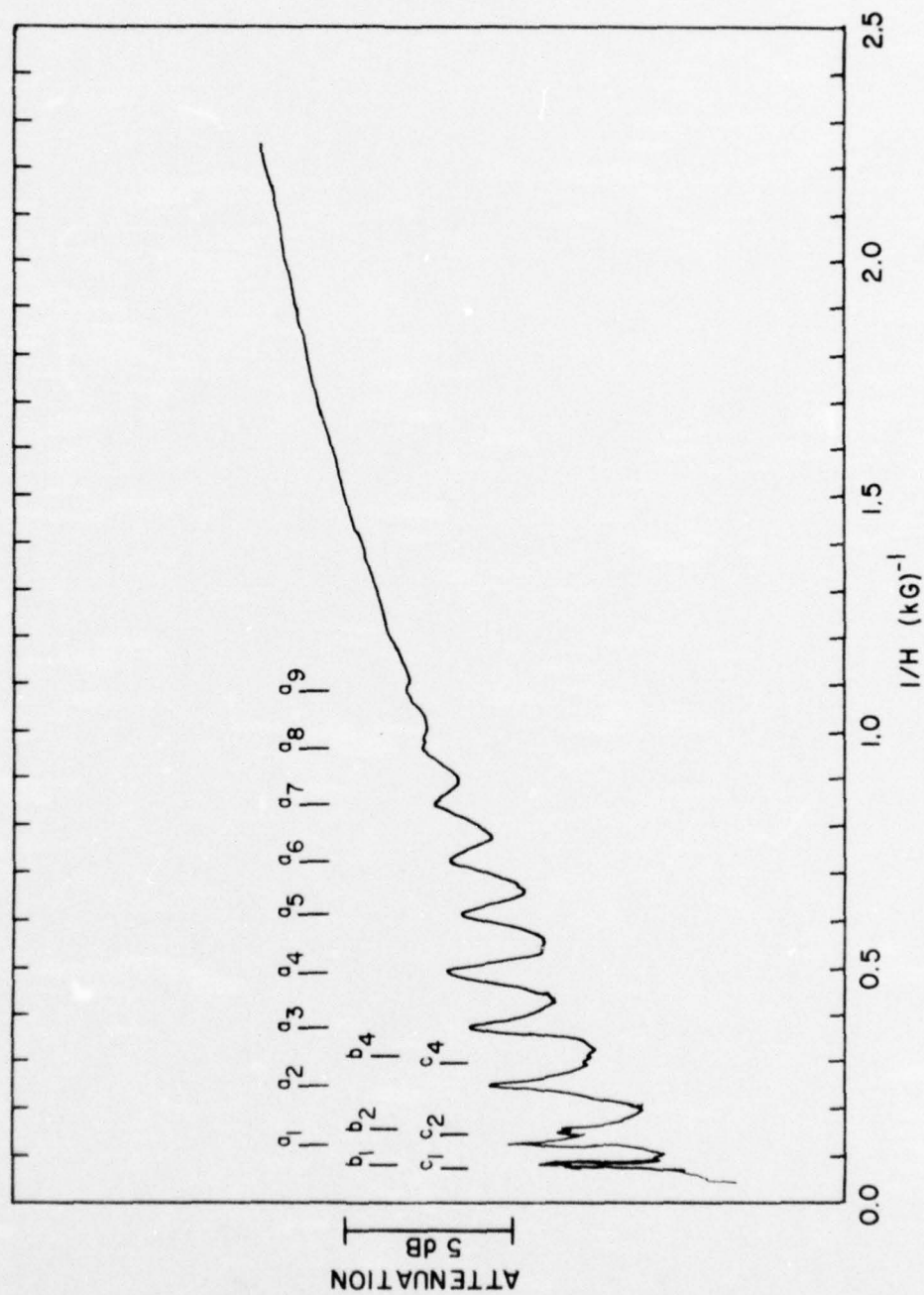


Figure 12. A Calcomp plot used in the determination of periodicity in $1/H$.

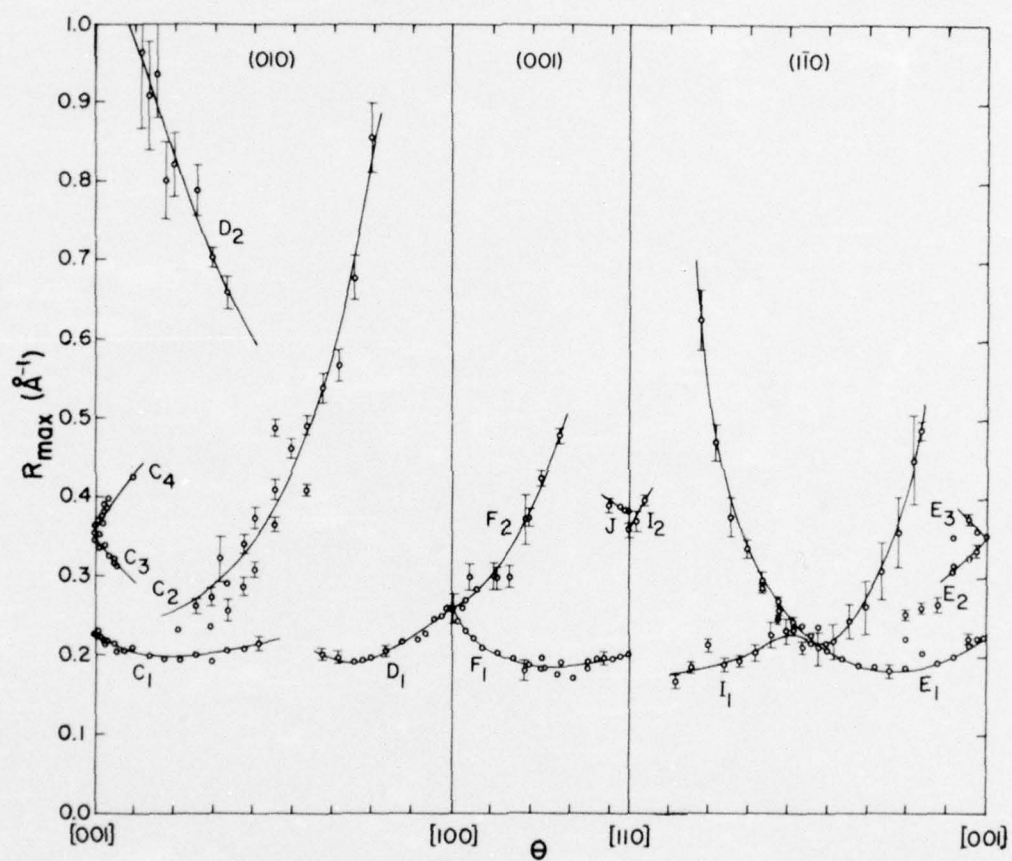


Figure 13. Values of R_{\max} , calculated from the experimental data, plotted against θ , the angle between \vec{q} and \vec{H} .

TABLE I. Experimental values of R_{\max} along axes of crystal symmetry.

Axis	$R \text{ (}\overset{\circ}{\text{A}}^{-1}\text{)}_{\max}$	
[001]	0.225	0.353
[100]	0.262	-
[110]	0.199	0.364

The error bars in Figure 13 represent estimated uncertainties arrived at in the following way. A standard deviation was calculated for each least-mean-square fit of $\Delta(1/H)$ values to n for a particular series which took into consideration errors in scaling with a ruler the plots like the one shown in Figure 12. For large angles between \vec{q} and \vec{H} , most of the uncertainty arises from the uncertainty in the orientation of a specimen. Since, according to Equation (23) in Chapter II, the value of R_{\max} is inversely proportional to the cosine of the angle between \vec{q} and \vec{H} , the error in R_{\max} due to misorientation is equal to $(\tan \theta)\Delta\theta$. It is estimated that the specimens are orientated to within 1° of a principal crystal direction. The uncertainty in the magnet calibration, which was estimated to be less than 0.3%, was considered negligible. The time lag in the lock-in amplifier also was negligible because the lock-in time constant was set to a value much shorter than the minimum time between passage of the resonance peaks which was determined by the time-rate of sweep of the magnetic field.

Comparison of the Results with Models of the Fermi Surface of Indium

The selection rule for n , the order index of a resonance, was discussed in Chapter II. Its relation to the experimental values of R_{\max} when \vec{H} was parallel to a direction of crystal symmetry (the [001], [100], and [110] directions in Figure 13) is considered here. The selection rule has been observed in gallium.³³ The fundamental ($n = 1$) and odd harmonic resonance peaks were reduced in amplitude by a factor typically the order of 20 when \vec{H} and \vec{q} were in a direction of an axis of symmetry. When the angle between \vec{H} and \vec{q} was greater than approximately 1° (\vec{q} along the symmetry axis), the amplitude of the resonance for an odd-integer n was large enough to be easily observed. In the present investigation, also, decreases in amplitude were observed, but not by factors as large as those reported for gallium. It may be that misorientations of our specimens within the estimated uncertainty of 1° can account for our not observing greater differences in the magnitude of the odd and even numbered resonances. All the curves in Figure 13 with the exception of J, in the [110] direction, extend more than 5° from the axis of crystal symmetry where resonance absorption peaks for all values of n , even and odd, are expected. Since our values of R_{\max} at and near a symmetry axis are continuous with the values well displaced from the axis, it is believed that the values of R_{\max} along crystal axes given in Table I are not in need of any adjustment because of the selection rule on n . The curve J in Figure 13, also, requires no modification for the n -selection rule since some of the values of R_{\max} on the J-curve were obtained using a specimen

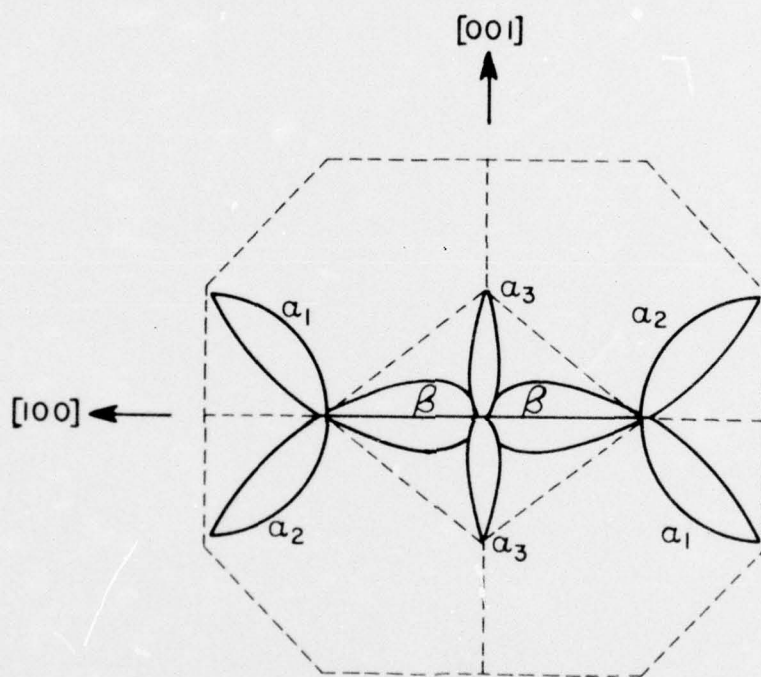
in which \vec{q} was parallel to the [100] axis making the angle between \vec{q} and \vec{H} about 45° for these J-curve points.

Comparing Figures 9 and 13, it is evident that the values of R_{\max} measured in this investigation do not correspond with the experimentally verified values in the second zone calculated from the OSA model which includes all the curves in Figure 9 with the exception of those labeled A. Neither the values of R_{\max} along the principal crystal directions nor the variation of R_{\max} with angle between \vec{q} and \vec{H} (Figure 9) correspond. The values of R_{\max} for the curves C_2 and E_1 along the [001] direction (Figure 13) are within 4% of the OSA value for curve A in the (010) and (1 $\bar{1}$ 0) planes, respectively, in Figure 9. Curves A of Figure 9 represent $|\partial A(k_z)/\partial k_z|_{\max}$ for values of k_z near the Brillouin zone boundary and result from the rounding of the sharp corners of the second-zone Fermi surface in Figure 8. The shape of these calculated A-curves depends critically upon the choice of parameters for the pseudopotential model.³⁴ Since these A-curves have not been observed experimentally, it may be that their shape differs from that shown in Figure 9. However, it is expected that they would not extend more than roughly 45° from a symmetry direction as may be seen in Figure 8 of Chapter IV. Curves C_2 and E_1 extend 70° from the [001] direction making it unlikely that they correspond to curves A. The value of R_{\max} for F_2 (Figure 13) along the [100] direction is within 8% of the corresponding value for A and the variations of R_{\max} with angle between \vec{q} and \vec{H} in the (001) planes of Figures 9 and 13 are similar. Although it is unlikely that R_{\max} for the second-zone corners would be observed in the (001) plane and not in the (010)

and $(1\bar{1}0)$ planes, we include the identification of F_2 in Figure 13 with A in the (001) plane of Figure 9 as a remote possibility.

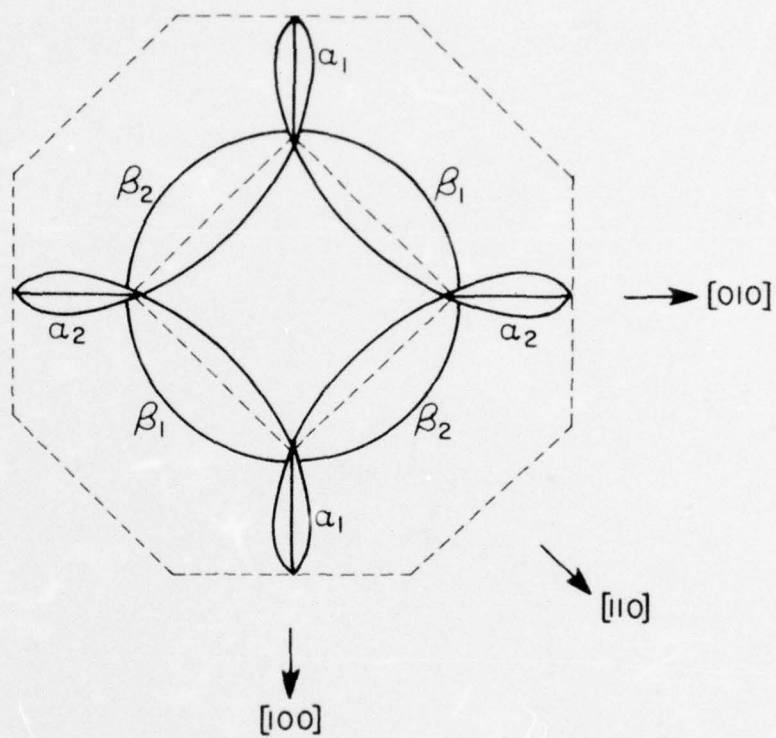
Interpretation of the data in terms of the third-zone Fermi surface is more successful provided the α -arms are assumed to exist and that the variation of R_{\max} with the angle between \vec{q} and \vec{H} has the general shape predicted by the free-electron model. This is apparent if the calculated free-electron values of R_{\max} in the (010) plane in Figure 10 are compared with the experimental data in Figure 13. C_1 and D_1 of Figure 13 were characterized by absorption peaks of large amplitude when compared with other data in the (010) plane and they contained up to the $n = 9$ resonance absorption peaks. It is possible that they arise from the same piece of the Fermi surface. If C_1 and D_1 are extended until they meet, they are similar to the α_1 curve in Figure 10. The shapes of curves C_2 and D_2 in Figure 13 are similar to α_3 (or α_2) and β respectively in Figure 10. Curves C_3 and C_4 of Figure 13, which were not identified in terms of the second-zone Fermi surface, are not identified in terms of the third zone either.

Although a free-electron calculation was not carried out for the (001) and $(1\bar{1}0)$ planes, the expected behavior of R_{\max} as a function of the angle between \vec{q} and \vec{H} can be estimated with the help of Figures 10 and 14. Figure 14a is the projection of the free-electron third zone Fermi surface on the (010) plane. When \vec{H} is along the $[100]$ direction, \vec{H} is in the plane containing the axes of the β -arms and R_{\max} is a minimum as shown in Figure 10. As \vec{H} is turned toward the $[001]$ direction in the (010) plane, R_{\max} increases, becoming large as \vec{H} approaches the $[001]$ direction. This is explained by the cross-



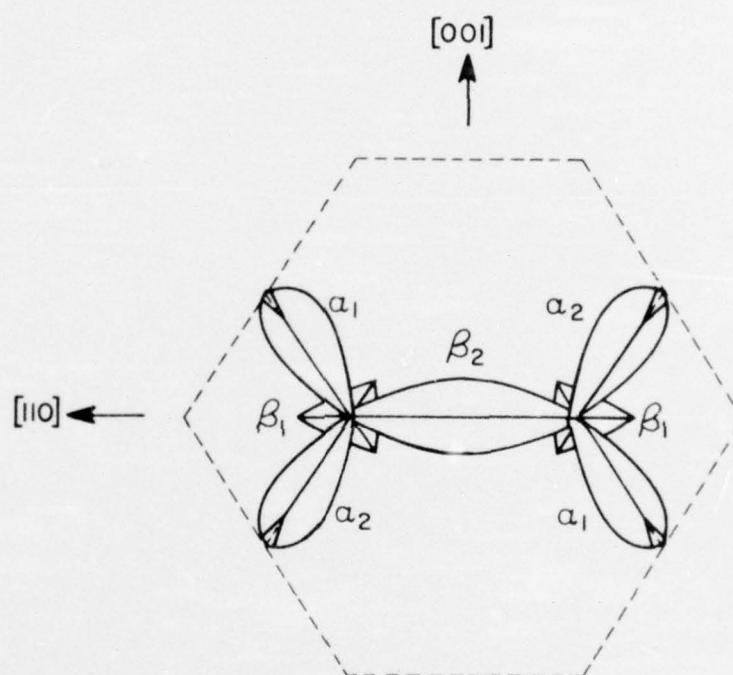
a. (010) plane.

Figure 14. Projections of the free-electron third-zone Fermi surface on crystal planes.



b. (001) plane.

Figure 14 (cont.)



c. (110) plane.

Figure 14 (cont.)

sectional area, $A(k_H)$, of the β -arms becoming smaller at an increasing rate as k_H increases. Here k_H is the component of \vec{k} in the direction of \vec{H} . The value of R_{\max} is of the order of the ratio $A(k_H = 0)/k'_H$ where k'_H is the value of k_H where $A(k_H)$ becomes zero. For the α -arms a similar type of behavior is predicted. The curve α_1 of Figure 10 represents the behavior of α_1 in Figure 14a. When \vec{H} is at approximately 45° from the [001] direction, which corresponds to \vec{H} along the axes of the α_1 -arms, R_{\max} has a minimal value. Since c/a for indium deviates 8% from a face-centered cubic lattice value, the value of R_{\max} for the α_1 -arms is slightly larger along the [100] direction than along the [001] direction. This also accounts for the fact that the minimal value of R_{\max} is not exactly at 45° . The α_2 and α_3 -arms behave in a similar fashion. R_{\max} for the α_2 -arms becomes large at \vec{H} nearly 45° from the [001] direction which occurs when \vec{H} is normal to the α_2 axes and R_{\max} has the same value as for the α_1 -arms along the [001] and [100] directions. R_{\max} for the α_3 -arms becomes large as \vec{H} is varied from the [001] to the [100] directions.

The behavior of R_{\max} for the α and β -arms can now be predicted in the (001) and (110) planes. Figure 14b is the projection of the third-zone Fermi surface on the (001) plane. In this plane, as \vec{H} is varied from the [100] to the [110] directions, R_{\max} for the β -arms labeled β_1 is expected to decrease, reaching a minimum value when \vec{H} is parallel to the axes of the β_1 -arms; that is, parallel to the [110] direction. This corresponds to \vec{H} turning to a direction normal to the axes of the β_2 -arms so that R_{\max} for β_2 should become large. This is the behavior exhibited by F_1 and F_2 in Figure 13. However, F_1 is the extension of

the same series of resonance peaks along the $[100]$ direction in the (001) plane as D_1 in the (010) plane. Since D_1 was identified with an α -arm, to be consistent, F_1 should also be identified with an α -arm. Since it is not a likely coincidence that R_{\max} for an α -arm would equal R_{\max} for a β -arm along a symmetry direction, F_2 would correspond to an α -arm. Further, in the (010) plane there was no evidence of β -arm data near the $[100]$ direction. It is possible that the arms labeled α_1 in Figure 14b could correspond to F_1 but the assignment of F_2 to an α -arm does not seem to be possible. The resonance absorption peaks for the F_1 series were large whereas the resonance absorption peaks for the F_2 series were small and were difficult to analyze as is evidenced by the large error bars for F_2 in Figure 13. It may be that F_2 was incorrectly identified as a series. The curve J of Figure 13 might possibly correspond to R_{\max} for the β -arms near the $[110]$ direction.

Figure 14c is the projection of the third-zone Fermi surface on the $(1\bar{1}0)$ plane. When \vec{H} is in the $[110]$ direction, R_{\max} for β_1 is large whereas R_{\max} for β_2 is a minimum. R_{\max} for β_2 grows large as \vec{H} approaches the $[001]$ direction. For α_1 , the variation of R_{\max} is expected to be like that for α_1 in Figure 14a; that is, reaching a minimum when θ is nearly 45° . R_{\max} for α_2 is expected to become large as θ approaches 45° from both the $[110]$ and $[001]$ directions and behave much like α_2 of Figure 14a. In Figure 13, I_2 might correspond to β_2 and be an extension of J into the $(1\bar{1}0)$ plane. Using the same argument by which F_1 was attributed to an α -arm because D_1 was assigned to an α -arm, E_1 along the $[001]$ direction must be attributed to an α -arm since it is the extension of C_1 into the $(1\bar{1}0)$

plane and C_1 was attributed above to an α -arm. The amplitude of the E_1 series was large for \vec{H} parallel to the $[001]$ direction. However, as \vec{H} was turned towards the $[110]$ direction, the amplitude of the absorption peaks diminished rapidly and became so small that they were difficult to analyze. When 28° was reached, a series of resonances of large amplitude appeared with a periodicity, $\Delta(1/H)$, nearly the same as for θ less than 28° . It is possible E_1 corresponds to two different pieces of the Fermi surface; that is, α_1 of Figure 14c for θ less than 28° and an as yet unidentified piece for θ greater than 28° . I_1 and I_2 data were taken using the specimen in which \vec{q} was parallel to the $[110]$ direction. In this specimen, the amplitudes of the absorption peaks were only slightly above the noise level when θ was less than 10° and only I_2 and J were observed in this specimen. F_1 data near the $[110]$ direction in the (001) plane were taken using the specimen in which \vec{q} was parallel to the $[100]$ direction. The amplitude of the I_1 series absorption peaks were small for θ less than 36° measured from the $[110]$ axis and were not observed near the $[110]$ direction. If I_1 for θ less than 36° is the extension of F_1 into the $(1\bar{1}0)$ plane it would correspond to an α -arm. Analogous to the behavior for E_1 , the amplitudes of the absorption peaks of the I_1 series were large and were easily analyzed when θ was greater than 36° . The series E_1 for θ greater than 28° measured from the $[001]$ direction and I_1 for θ greater than 36° measured from the $[110]$ direction exhibit large amplitude absorption resonances and might arise from the same piece of the Fermi surface. β_1 in Figure 14c has the same symmetry as the curve formed by joining curve E_1 to I_1 in

Figure 13 at θ equals 45° . It is possible that E_1 joined to I_1 at 45° does correspond to R_{\max} for the β_1 -arms. E_2 and E_3 are extensions of C_3 and C_4 into the $(1\bar{1}0)$ plane and they have not been related to the Fermi surface.

In summary, it appears that the assignment of the DSACR data, Figure 13, to the third-zone piece of the Fermi surface is the one most consistent with all the data. It assumes the existence of α -arms. It appears that the curves C_1 and D_1 in Figure 13, for which the absorption peaks are among the largest amplitude measured in this investigation, can be attributed only to α -arms. Existing pseudopotential calculations of the Fermi surface of indium are based on the assumption that the α -arms are nonexistent in indium. Calculations from these pseudopotentials would not, therefore, be expected to be reliable even for the β -arms. If our assignment of the DSACR data is correct, it has important implications for the size and shape not only of the α -arms of the Fermi surface in indium but the β -arms as well.

Dependence of the DSACR Attenuation on Temperature, Magnetic Field, and Sonic Frequency

A theory for the Doppler-shifted acoustic cyclotron resonances which relates the height of the acoustic resonance absorption peaks to the temperature of the specimen, the magnitude of the magnetic field, and the sonic frequency has not been developed. A limited experimental investigation was made of the effects of temperature, magnetic field, and sonic frequency on the size of the acoustic resonance peaks. The results are shown in Figures 15 to 17. In these figures, Δ represents

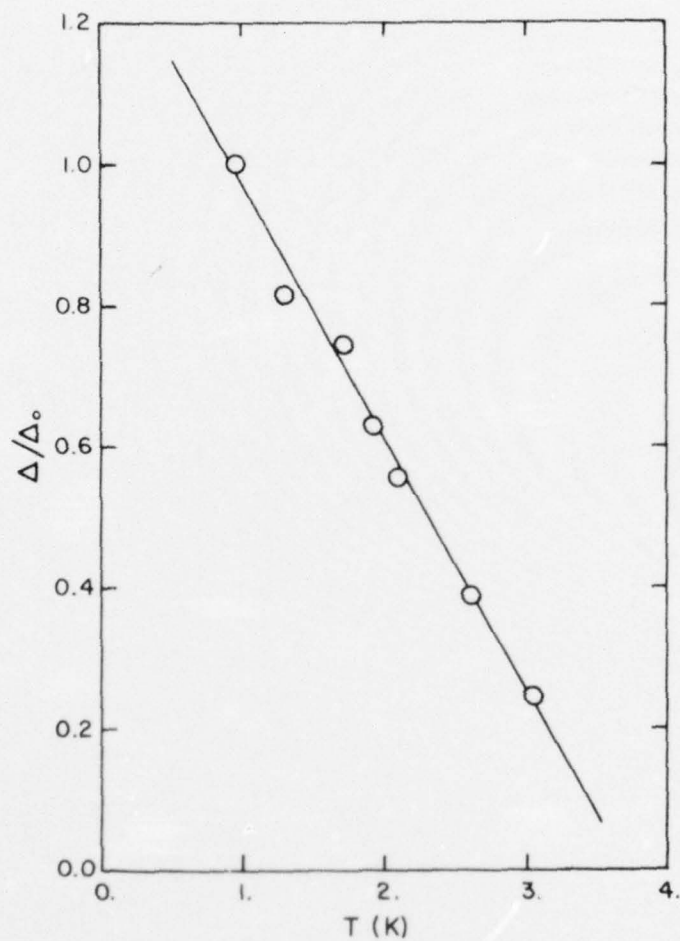


Figure 15. Normalized height of the absorption peak, Δ/Δ_0 , vs. temperature.

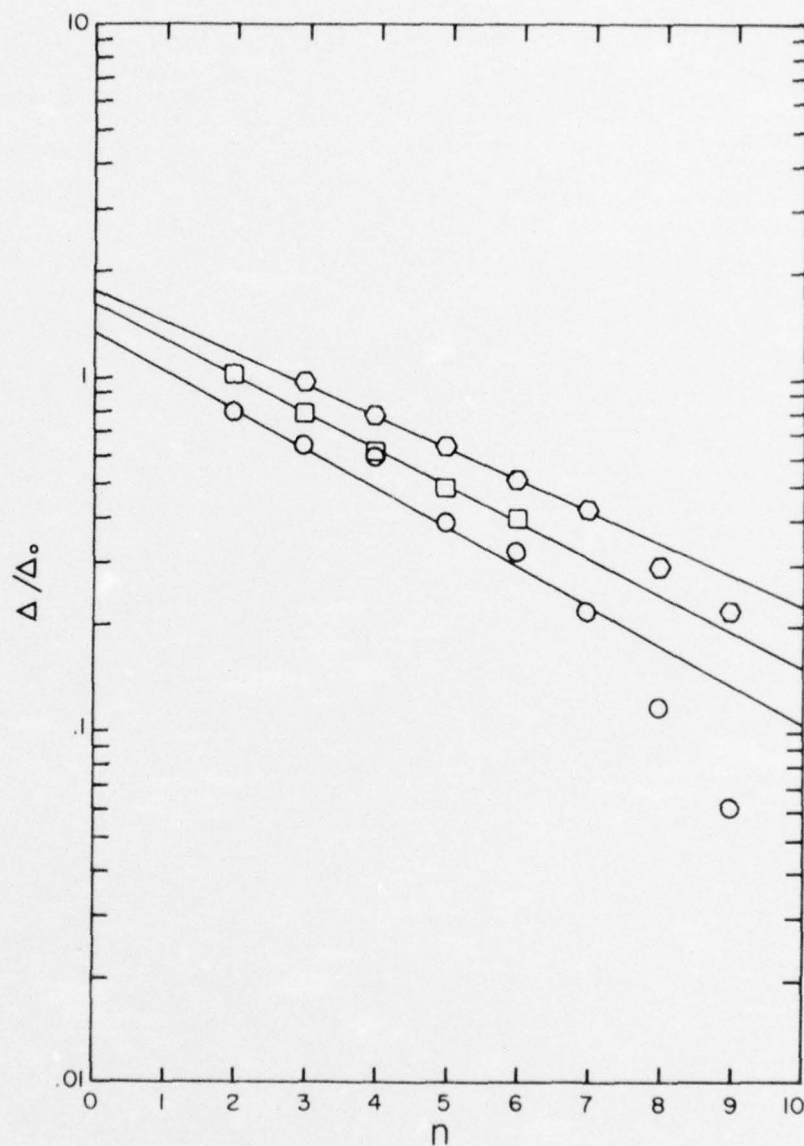


Figure 16. The normalized height of the absorption peaks, Δ/Δ_0 , on a logarithmic scale vs. the order number, n , of the peaks.

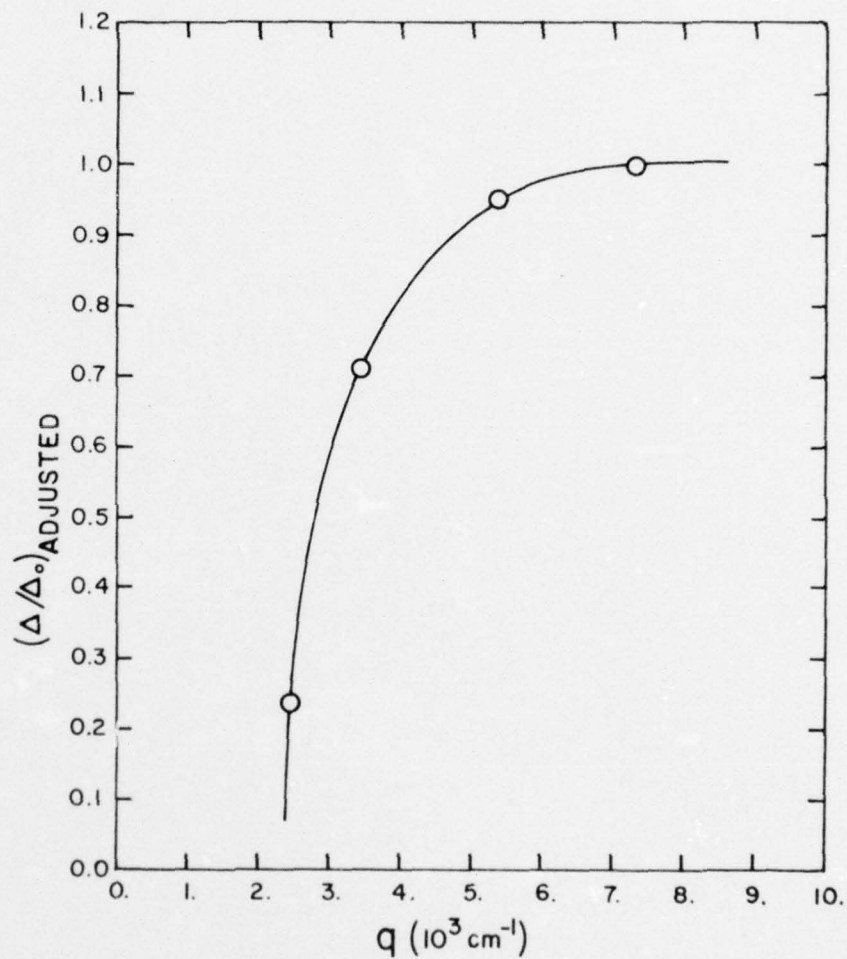


Figure 17. The normalized height of the absorption peaks, Δ/Δ_0 , vs. sonic wave number, q .

the height of a resonance absorption peak in decibels relative to the background attenuation; that is, Δ equals $(\alpha - \alpha_b)$ where α is the peak (total) ultrasonic attenuation and α_b is the background ultrasonic attenuation (for the same value of H) above which the DSACR absorption peak rises. For Figures 15 to 17, Δ_0 is the largest recorded value of Δ for the figure.

Δ was determined by scaling the P.S.U. Calcomp attenuation versus $(1/H)$ plots of which Figure 12 is an example. For this purpose, the output of the lock-in amplifier (Figure 5d), which is measured in voltage units, was calibrated in db. Calibrated attenuators were inserted in the receiving circuit ahead of the logarithmic amplifier (Figure 5a). An attenuator reduced the output voltage by a fraction that was practically independent of the output voltage over the entire useful range of voltages,

$$(\text{attenuation in dB}) = 20 \log_{10} (V_1/V_2) \quad (1)$$

Thus, while the receiver output was not readable in attenuation in decibels, differences or changes in output voltage were, after calibration, precisely readable in dB. Sonic attenuation resulting from transducer bonds, thermal phonons, crystal impurities and imperfections, which do not change when parameters like H and θ are varied, do not affect the value of Δ .

Figure 15 is a plot of Δ/Δ_0 data as a function of temperature. The $n = 2$ resonance absorption peak was selected for investigation. The sonic frequency was 220.8 MHz and \vec{q} was parallel to the $[110]$ direction;

\vec{H} was in the (001) plane displaced 10° from \vec{q} . Δ_0 for the $n = 2$ resonance was 5.86 dB at 0.98 K. The linear relationship

$$\Delta/\Delta_0 = mT + b \quad (2)$$

is evident in Figure 15. For this absorption peak, $m = (-0.36 \pm 0.02)K^{-1}$ and $b = (1.33 \pm 0.04)$.

Figure 16 is a plot of Δ/Δ_0 on a logarithmic scale as a function of the order number of the resonance peak, n . Three separate resonance series are plotted in Figure 16 distinguished by a hexagon, square, and circle which are referred to as A, B, and C respectively. Information pertinent to each is given in Table II. Δ_0 was Δ for the $n = 2$ resonance peak of B and equaled 9.55 dB. For values of n less than or equal to seven, the curves are linear and can be expressed by

$$\ln (\Delta/\Delta_0) = mn + b \quad (3)$$

or

$$\Delta/\Delta_0 = Ke^{-mn}, \quad (4)$$

where $K = e^b$. The values for m and K are given in Table II. The values of m are nearly equal. Since the resonance peaks are periodic in $1/H$, Figure 16 is equivalent to a plot of $\log (\Delta/\Delta_0)$ vs. $1/H$. For n less than or equal to seven the curves may be represented by

$$\Delta/\Delta_0 = Ke^{-m'/H}, \quad (5)$$

where $m' = m/\Delta(1/H)$. The values of m' also are given in Table II. The $n = 1$ points for curves B and C and the $n = 1$ and $n = 2$ points for A are missing from the plot since for small values of $1/H$ the

TABLE II. Information pertinent to the investigation of the dependence of Δ/Δ_0 on temperature and magnetic field. A, B, and C correspond to the curves of Figure 16. The columns labeled \vec{q} , \vec{H} and θ indicate the orientation of \vec{q} and \vec{H} where θ is the angle between \vec{q} and \vec{H} .

\vec{q}	\vec{H}	$\theta(^{\circ})$	$\Delta(1/H) \text{ (kG)}^{-1}$	$f \text{ (MHz)}$	m	k	$m' \text{ (kG)}$
A [001]	(110)	1.6	0.1275 ± 0.0002	304.8	0.210 ± 0.002	1.82 ± 0.02	1.65 ± 0.02
B [100]	(010)	0.0	0.09455 ± 0.00008	261.0	0.232 ± 0.006	1.58 ± 0.03	2.45 ± 0.07
C [001]	(010)	44.0	0.1235 ± 0.0002	223.2	0.25 ± 0.02	1.4 ± 0.1	2.0 ± 0.2

background attenuation was difficult to determine and no reliable measurement of Δ could be made. For n greater than seven, the data departs from the straight lines in Figure 16. Δ was difficult to measure for large values of n , but it appears that the linear relation represented in Equation (5) fails for large values of n (small values of H).

Figure 17 is a plot of Δ/Δ_0 versus the sonic wave number, q , which is proportional to the sonic frequency. The $n = 3$ peak was measured and Δ_0 was 7.41 dB, the value of Δ for $q = 7.31 \times 10^3 \text{ cm}^{-1}$. The values of Δ/Δ_0 have been adjusted for the fact that the resonance absorption peaks for different sonic frequencies occur at different values of magnetic field (see Equation (23) in Chapter II). Using the average value of m in Table II, the adjusted value of Δ/Δ_0 was calculated on the false assumption that all the resonance absorption peaks occurred at the same value of H , namely the value of H for the peak with q equal to $7.31 \times 10^3 \text{ cm}^{-1}$. q was parallel to the $[001]$ direction and \vec{H} was in the $(1\bar{1}0)$ plane at an angle of 68° from \vec{q} . The temperature was 1 K.

It is to be expected that DSACR would not be observable if the product $q\ell$, where ℓ is the electron mean-free-path, was less than one. In Figure 17, Δ approaches zero at q equal to $2 \times 10^3 \text{ cm}^{-1}$. Since for the indium used in this investigation was $\sim 10^{-3} \text{ cm}$ (see Appendix A), the critical value of $q\ell$ for the appearance of DSACR absorption peaks in Figure 17 is 2.

CHAPTER VI

SUMMARY, CONCLUSIONS, AND SUGGESTIONS FOR FUTURE WORK

The purpose of this investigation was to explore the Fermi surface of indium using DSACR and to make a limited investigation of the effect of some experimental parameters on the height of the DSACR absorption peaks.

DSACR absorption peaks were observed and they were interpreted in terms of the existing models of the Fermi surface of indium. The dependence of the height of the absorption peaks on temperature, magnetic field, and sonic wave number was measured and displayed graphically.

In order to accomplish these objectives some modifications of an existing experimental apparatus were made to make the recording of DSACR data more convenient. Since the existing local pseudopotential models of the Fermi surface of indium, which were deduced from other types of measurements, did not adequately account for the observations of this investigation, an extensive free-electron model calculation of the Fermi surface of indium in the third Brillouin zone was made and the results included. These calculations facilitated the interpretation of the experimental results.

It is hoped that the results of this investigation will contribute to the resolution of the problems concerning the Fermi surface of indium. An important concern is whether or not third-zone α -arms really exist. The free-electron model of indium includes them. However, in several investigations where it is expected α -arms would be

observed if they existed, there was no evidence for their existence. Other investigations, fewer in number, give evidence for α -arms but this evidence is questioned by some investigators. Pseudopotential calculations were made based on experimental data for the β -arms assuming the α -arms do not exist. However, small changes in the pseudopotential parameters can be made that would lead to α -arms without much effect on the β -arms. The small changes have been rejected since the α -arms are not generally observed.

The second-zone Fermi surface has been experimentally observed by other methods. It is evident that there is an absence of DSACR data in this investigation that corresponds to the second-zone surface. The most consistent interpretation of the data reported here is made in terms of the third-zone Fermi surface of indium including the α -arms. The evidence is good that some of the data arise from the β -arms but it appears that some of the best data can only arise from the α -arms. It is concluded then that the α -arms most probably do exist in pure indium.

Suggestions for Future Work

A calculation of R_{\max} for the β -arms of indium using the existing local pseudopotential models for indium should be helpful in testing the assignments made of the experimental data from this investigation, in particular those assignments made to β -arms. Also it would probably settle questions as to whether the assignments made here to α -arms might have been made instead to β -arms. After this use of existing pseudopotentials, a new local pseudopotential could be set up to include

the data of this investigation along with the other data. With this improved potential, the assignments of the DSACR data here could be made with more assurance.

A detailed theory of DSACR absorption that would explain the observed behavior of the resonance absorption peak heights under changes of temperature, magnetic field, and sonic frequency is needed. Such a theory would be constructed on the bases of the conductivity tensor and the deformation potentials for the Fermi surface.

APPENDIX A

PROPERTIES OF INDIUM

Physical data for indium relevant to the present work.

Atomic number:

$$A = 49$$

Atomic weight:

$$M = 114.82 \text{ g/mole}$$

Density at 20°C:

$$D = 7.31 \text{ gm/cm}^3$$

Electrical resistivity:

$$\rho(0^\circ\text{C}) = 8.37 \times 10^{-6} \text{ } \Omega\text{-cm}$$

Fermi energy (free-electron gas):

$$\epsilon_F = 1.40 \times 10^{-11} \text{ erg} = 8.74 \text{ e.v.}$$

Radius of the free-electron Fermi sphere in \vec{k} -space:

$$k_F = \frac{1}{h} (2m\epsilon_F)^{1/2} = 1.514 \times 10^8 \text{ cm}^{-1}$$

Fermi velocity for the free-electron gas:

$$v_F = \frac{\hbar k_F}{2m} = 1.75 \times 10^8 \text{ cm/sec}$$

Residual resistivity ratio for the indium used in this investigation:

$$\rho(300\text{K})/\rho(4.2\text{K}) = 8950 \pm 450$$

Electron mean-free-path at 4.2K (calculated):³⁵

$$\ell = \frac{\rho(300K)/\rho(4.2K)}{\rho(300K)} \frac{(m^* v_F)}{Ne^2} \approx 10^{-3} \text{ cm},$$

where N = density of the conduction electrons in indium and $m^* v_F$
 $\approx \hbar R \approx 2.64 \times 10^{-20}$ erg-sec/cm, a typical value taken from this research.

Product of the sonic wave number and the electron mean-free-path

$$q\ell (f = 300 \text{ MHz}) = 7$$

Ultrasonic velocities for longitudinal sonic waves at 4.2K:³⁶

$$v_s [001] = 2.62 \times 10^5 \text{ cm/sec}$$

$$v_s [100] = 2.68 \times 10^5 \text{ cm/sec}$$

$$v_s [110] = 2.90 \times 10^5 \text{ cm/sec}$$

APPENDIX B

FAST FOURIER TRANSFORM

The subroutine RHARM in the IBM "Scientific Subroutine Package" computes the Fourier coefficients $a_0, a_1, b_1, a_2, b_2, \dots, a_{N-1}, b_{N-1}$, and a_N in the equation

$$X_j = (1/2)a_0 + \sum_{k=1}^{N-1} [a_k \cos(\pi j k / N) + b_k \sin(\pi j k / N)] + (1/2)a_N (-1)^j, \quad (1)$$

where $j = 0, 1, 2, \dots, 2N-1$ and $2N$ is the number of dependent variables, X_j , corresponding to the equally spaced independent variables, $\pi j k / N$, and $2N$ is an integral power of two. For convenience, consider the case for a single frequency though the results that follow are general. Then, the data to be analyzed have the form

$$f(t) = \sin(2\pi v_0 t + \phi) = \sin(2\pi v_0 t) \cos(\phi) + \cos(2\pi v_0 t) \sin(\phi), \quad (2)$$

where v_0 is the value sought. Since j labels the independent variable $\pi j k / N$ with which the variable X_j is associated, it corresponds to t in Equation (2). Let t_L be the lower bound on t and t_U the upper bound so that $t(j = 0) = t_L$ and $t(j = 2N-1) = t_U$. Therefore,

$$j = (t - t_L) / \Delta t, \quad (3)$$

where

$$\Delta t = (t_U - t_L) / 2N, \quad (4)$$

the increment in the independent variable. Then we can write

$$2\pi v_0 t = \pi j k / N = (\pi k (t - t_L)) / N \Delta t \quad (5)$$

or

$$v_0 = (k/t) [(t - t_L) / \Delta t] \quad (6)$$

where

$$\Delta T = t_U - t_L \quad (7)$$

the total range of the independent variable. We can set $t_L = 0$ which will only affect ϕ in Equation (2) and, hence, does not affect the calculation of v_0 . Then

$$v_0 = k / \Delta T \quad (8)$$

or

$$k = \Delta T v_0 \quad (9)$$

Define the resolution, R , as the difference in v_0 between adjacent values of k . Then

$$R \equiv v_0(k+1) - v_0(k) = 1 / \Delta T \quad (10)$$

Hence, the resolution, R , is independent of the number of points used and depends only on the total range of the independent variable. The number of points used does affect the range of v_0 . From Equation (8),

$$v_0(\min) = 0 \quad (11)$$

and

$$v_0(\max) = (N-1) / \Delta T = N / \Delta T = 1 / (2 \Delta t) \quad (12)$$

Hence, the minimum period which can be analyzed equals twice the interval between the independent variables for large N .

FOOTNOTES

- ¹E. A. Kaner, V. G. Peschanskii and I. A. Privortski, Sov. Phys., JETP 13, 147 (1961).
- ²E. A. Kaner, Sov. Phys., JETP 16, 154 (1963).
- ³G. L. Kotkin, Sov. Phys., JETP 14, 201 (1962).
- ⁴J. Mertsching, Phys. Status Solidi 37, 465 (1970).
- ⁵S. Raimes, The Wave Mechanics of Electrons in Metals (North-Holland Publishing Co., Amsterdam, 1967) Chapter 11.9.
- ⁶S. W. Hui and J. A. Rayne, J. Phys. Chem. Solids 33, 611 (1972).
- ⁷S. G. Eckstein, Phys. Rev. Letters 16, 611 (1966).
- ⁸Mertsching, loc. cit.
- ⁹Kotkin, loc. cit.
- ¹⁰R. W. Reed and F. G. Brickwedde, Phys. Rev. B 3, 1081 (1971).
- ¹¹The multi-ramp sweep and high-speed sample and hold circuits were designed and constructed by R. W. Reed.
- ¹²R. W. Reed, D. E. Binnie and F. G. Brickwedde, J. Acous. Soc. Amer. 51, 910 (1971).
- ¹³The residual resistance ratio measurements were made by Mr. Edward F. Vozenilek.
- ¹⁴C. S. Burett, Advances in X-ray Analysis (Plenum Press, Inc., New York, 1962), v 5, p. 33.
- ¹⁵W. A. Harrison, Phys. Rev. 118, 1190 (1960).
- ¹⁶J. A. Rayne, Phys. Rev. 129, 652 (1963).
- ¹⁷V. F. Gantmakher and I. P. Krylov, Sov. Phys., JETP 22, 736 (1966).
- ¹⁸R. T. Mina and M. S. Khaikin, Sov. Phys., JETP 21, 75 (1965).
- ¹⁹R. T. Mina and M. S. Khaikin, Sov. Phys., JETP 24, 42 (1966).
- ²⁰W. J. O'Sullivan, J. E. Schirber and J. R. Anderson, Phys. Lett. 27A, 144 (1968).
- ²¹G. B. Brandt and J. A. Rayne, Phys. Lett. 12, 87 (1964).

- ²²Rayne, loc. cit.
- ²³O'Sullivan, et.al., loc. cit.
- ²⁴H. J. Trodahl, J. Phys. C: Solid St. Phys. 4, 1764 (1971).
- ²⁵Ibid.
- ²⁶A. J. Hughes and J. P. G. Shepherd, J. Phys. C: Solid St. Phys. 2, 661 (1969).
- ²⁷N. W. Ashcroft and W. E. Lawrence, Phys. Rev. 175, 938 (1968).
- ²⁸Ibid.
- ²⁹See for example H. W. Hayden, W. G. Moffatt and J. Wulff, The Structure and Properties of Materials, (John Wiley and Sons, Inc., New York, 1965), Volume III, Sections 4.8 and 5.3.
- ³⁰G. B. Brandt and J. A. Rayne, Phys. Rev. 132, 1512 (1963).
- ³¹R. W. Reed and F. G. Brickwedde (to be published).
- ³²Harrison, loc. cit.
- ³³J. A. Munarin, Phys. Rev. 172, 737 (1968).
- ³⁴Trodahl, loc. cit.
- ³⁵Calculated from the free-electron definition of conductivity and relaxation time. See for example, J. P. McKelvey, Solid-State and Semiconductor Physics (Harper and Row, New York, 1966), Section 7.3.
- ³⁶D. E. Binnie, Ph.D. Thesis, (1971), The Pennsylvania State University, entitled "Ultrasonic Attenuation in Superconducting Indium and Indium-Tin Alloys", p. 69.

BIBLIOGRAPHY

BOOKS

Burett, C. S., Advances in X-ray Analysis, Plenum Press, Inc., New York, 1962.

Hayden, H. W., W. G. Moffatt and J. Wulff, The Structure and Properties of Materials. Volume III. John Wiley and Sons, Inc., New York, 1965.

McKelvey, J. P., Solid-State and Semiconductor Physics. Harper and Row, New York, 1966.

Raimes, S., The Wave Mechanics of Electrons in Metals. North-Holland Publishing Co., Amsterdam, 1967.

ARTICLES

Ashcroft, N. W. and Lawrence, W. E., "Fermi Surface and Electronic Structure of Indium," The Physical Review 175, 938 (1968).

Brandt, G. B. and Rayne, J. A., "Low-Field de Haas-van Alphen Effect in Indium," The Physical Review 132, 1512 (1963).

Brandt, G. B. and Rayne, J. A., "De Haas-van Alphen Effect in Indium," Physics Letters 12, 87 (1964).

Eckstein, S. G., "Magnetoacoustic Antiresonance," Physical Review Letters 16, 611 (1966).

Gantmakher, V. G. and Krylov, I. P., "Radio-Frequency Size Effect in Indium," Soviet Physics JETP 22, 736 (1966).

Harrison, W. A., "Electronic Structure of Polyvalent Metals," The Physical Review 118, 1190 (1960).

Hughes, A. J. and Shepherd, J. P. G., "De Haas-van Alphen Measurements and the Band Structure of Indium," Journal of Physics C:Solid State Physics 2, 661 (1969).

Hui, S. W. and Rayne, J. A., "Doppler-Shifted Acoustic Cyclotron Resonance in Tungsten," Journal of the Physics and Chemistry of Solids 33, 611 (1972).

Kaner, E. A., "Theory of Acoustic Cyclotron Resonance in Metals," Soviet Physics JETP 16, 154 (1963).

Kaner, E. A., Peschanski, V. G. and Privorotski, I. A., "Contribution to the Theory of Magnetoacoustic Resonance in Metals," Soviet Physics JETP 13, 147 (1961).

Kotkin, G. L., "Contribution to the Theory of Absorption of Ultrasonic Waves by Metals in a Magnetic Field," Soviet Physics JETP 14, 201 (1962).

Mertsching, J., "Theory of Electromagnetic Waves in Metals and their Interaction with Ultrasonic Waves (III)," Physica Status Solidi 37, 465 (1970).

Mina, R. T. and Khaikin, M. S., "Investigation of the Fermi Surface of Indium," Soviet Physics JETP 21, 75 (1965).

Mina, R. T. and Khaikin, M. S., "Investigation of the Fermi Surface and of Carrier Velocities in Indium by the Cyclotron Resonance Method," Soviet Physics JETP 24, 42 (1966).

Munarin, J. A., "Doppler-Shifted Acoustic Cyclotron Resonance in Gallium," The Physical Review 172, 737 (1968).

O'Sullivan, W. J., Schirber, J. E. and Anderson, J. R., "de Haas-van Alphen Study of the 2nd Zone Hole Surface of In," Physics Letters 27A, 144 (1968).

Rayne, J. A., "High-Frequency Magnetoacoustic Measurements in Indium and Lead," The Physical Review 129, 652 (1963).

Reed, R. W., Binnie, D. E. and Brickwedde, F. G., "An Amplifier Gain Control for Ultrasonic Pulse-Echo Measurements," The Journal of the Acoustical Society of America 51, 910 (1971).

Reed, R. W. and Brickwedde, F. G., "Magnetoacoustic Absorption of Longitudinal Sound in Magnesium in High Magnetic Fields," The Physical Review B 3, 1081 (1970).

Trodahl, H. J., "The Sondheimer Size Effect in Indium Single Crystals," Journal of Physics C:Solid State Physics 4, 1764 (1971).

THESIS

Binnie, D. E., "Ultrasonic Attenuation in Superconducting Indium and Indium-Tin Alloys," Doctoral Thesis in Physics, The Pennsylvania State University (1971).